Synapsing with oligodendrocyte precursor cells stop sensory axons regenerating into the spinal cord

Hyukmin Kim[1], Andy Skuba[1], Jingsheng Xia[2], Sung Baek Han[1], Jinbin Zhai[1], Rachel Yoo[1], Huijuan Hu[2], Shin H. Kang[1], and Young-Jin Son[1,*]

[1]Shriners Hospitals Pediatric Research Center, Department of Neural Sciences, Lewis Katz School of Medicine, Temple University, Philadelphia, PA

[2]Department of Medicine, New Jersey Medical School, Rutgers University, Newark, NJ

* Correspondence: Dr. Young-Jin Son, yson@temple.edu

ABSTRACT

Adult mammalian spinal cord stops re-entering sensory axons, resulting in incurable sensory loss after dorsal root injury. Challenging the prevailing view, we previously showed that axons rapidly stop by forming synaptic, not dystrophic endings, and that myelin inhibitors and CSPGs are not the primary mechanism arresting axons. Here, we report that in adult mice dystrophic endings are formed by occasional axons embedded in fibrous collagens, exclusively at the CNS:PNS boundary where oligodendrocyte precursor cells (OPCs, or NG2 glia) are sparse. Most axons stop beyond the boundary in extensive contacts with OPC processes. Live imaging, immuno-EM and OPC-DRG co-culture show that axonal synapses form on OPCs. Genetic OPC ablation, although incomplete, enables many axons to continue regenerating deep into the spinal cord. These data, together with earlier findings, conclusively demonstrate that axons stop largely because OPCs stimulate presynaptic differentiation. We identify OPCs as a major regenerative barrier at the CNS:PNS border.

INTRODUCTION

The dorsal root (DR) carries primary sensory axons projecting centrally from DR ganglia (DRG). DR injuries commonly result from brachial plexus trauma, causing incurable loss of sensation, uncoordinated movement and chronic pain (Kaiser et al., 2020). The devastating consequences are because DR axons stop regenerating at the entrance of the spinal cord, the dorsal root entry zone (DREZ), and therefore fail to restore connections with intraspinal neurons. Both neuron-intrinsic and -extrinsic inhibitors, which limit axon regrowth elsewhere in the injured CNS (He and Jin, 2016; Varadarajan et al., 2022), are believed to prevent re-entry of DR axons. Unlike direct CNS injury, DR injury damages axons in the PNS without causing an impassable glia scar. Nevertheless, DR axons stop at the scar-free DREZ, even after a nerve conditioning lesion that boosts regenerative ability (Chong et al., 1999; Di Maio et al., 2011).

How the scar-free DREZ or spinal cord stops axons remains unclear, but myelin-associated inhibitors and chondroitin sulfate proteoglycans (CSPGs) are conventionally considered responsible (Mar et al., 2016; Smith et al., 2012). Surprisingly, however, co-eliminating myelin inhibitors (Nogo/Reticulon-4, MAG, OMgp) and CSPGs enables only a few conditioning-lesioned axons to extend a short distance beyond the DREZ (Zhai et al., 2021). These findings led us to suggest that unknown mechanism(s), unrelated to myelin inhibitors and CSPGs, primarily account for the vigorous axon arrest at the CNS:PNS border.

Our earlier findings also challenged the notion that DR axons stop by forming dystrophic endings or retraction bulbs (Smith *et al.*, 2012), like severed CNS axons degenerating after spinal cord injury (Blanquie and Bradke, 2018; Hill, 2017). This prevalent notion was based on *in vitro* studies and on the large bulbous endings occasionally reported in light- or ultramicroscopic studies. The first *in vivo* imaging of regenerating DR axons, however, revealed that axons rapidly stop at the DREZ and remain completely immobilized, with only a few enlarging their tips. Furthermore, immobilized axons exhibited synaptic-like or apparent presynaptic endings that formed on unknown non-neuronal cells (Di Maio *et al.*, 2011). These findings led us to suggest that non-neuronal cells rapidly stop regenerating axons by eliciting presynaptic differentiation. We speculated that these cells may be oligodendrocyte precursor cells (OPCs), also known as

NG2 glia (Son, 2015), that form synapses with neurons widely in intact CNS (Bergles et al., 2000; Mount et al., 2019; Osterstock et al., 2018).

Here, we confirm that these non-neuronal, postsynaptic cells are OPCs and that their depletion enables axons to continue regenerating deep into the spinal cord. Additionally, we suggest that macrophages, astrocytes, pericytes, and Schwann cells are not directly involved in arresting axons, and that dystrophic endings form infrequently in the absence of OPC contacts. These findings provide new insights into the regeneration failure at the CNS:PNS border, and the pathophysiological significance of OPCs in the traumatized nervous system.

RESULTS

Dystrophic endings form by occasional axons embedded in collagen fibers at the borderline

Most DR axons do not stop regenerating at the peripheral boundary of the DREZ where astrocytes/oligodendrocytes are juxtaposed to Schwann cells, but cross the borderline and then stop in CNS territory, within ~100μm of the boundary (i.e., DREZ) (Di Maio *et al.*, 2011; Zhai *et al.*, 2021). Surprisingly, live imaging in adult mice revealed that DR axons rapidly stop as they enter the DREZ, and remain profoundly immobilized, even after a nerve-conditioning lesion (Di Maio *et al.*, 2011). More strikingly, ultrastructural surveys targeting immobilized axons disclosed synaptic profiles exhibiting obvious features of presynaptic differentiation [Figure 1A; (Di Maio *et al.*, 2011)]. Because we did not observe a retracting or dystrophic axon displaying a large disorganized ending, we extended our earlier work by expanding ultrastructural surveys to a broader area of the DREZ to look for the formation of dystrophic endings.

We crushed cervical roots of adult mice and prepared longitudinal slices of dorsal spinal cord containing a root at 2 wpi. These preparations facilitated distinguishing CNS and PNS territory along a long border under electron microscopy (EM; e.g., Figure 5C). Thorough searches of wide areas on numerous slices occasionally revealed large bulbous endings reminiscent of dystrophic endings or retraction bulbs. These endings were 3 to 5 times larger than axons and densely filled with disorganized multi-organelles and scattered vacuoles (Figure 1B). Notably, these dystrophic endings were usually observed near the boundary, but not in deeper CNS territory of the DREZ. Furthermore, unlike synaptic endings, these endings were embedded in collagen fibers and

displayed a notable absence of cellular contacts (Figure 1B). Similarly, dystrophic endings reported in earlier studies also lacked cellular contacts and were observed in PNS territory beyond the DREZ (Chong *et al.*, 1999).

We next employed light microscopic approaches to examine the incidence and location of dystrophic endings. In the first, we selectively labeled regenerating axons by microinjecting AAV2-GFP into DRGs after crushing cervical roots and assessed them in serial transverse sections at 2 wpi (Figure 1C). Some sections displayed large bulbous, presumptive dystrophic, endings (Figure 1C1, 4B, S3), which represented ~5% axons (Figure 1C2). Consistent with ultrastructural surveys, these endings were observed exclusively at or immediately near the borderline, but not deep in the CNS territory (Figure 1C3). Our second approach was to examine DR axons in their entirety without sectioning. To do this, we performed Clarity tissue clearing at 2 wpi, and examined fluorescently labeled axons in an entire root prepared in wholemounts (Figure 1D). High resolution 3D imaging of cleared roots revealed a small number of parent axons that turned around or formed dystrophic endings near the boundary. These axons represented ~15% and ~10% of all GFP+ axons, respectively (Figure 1D2). In contrast, most axons extended further and then stopped by forming small endings and frequent swellings on their shafts resembling varicosities (Figure 1d’, inset d'-3). Collectively, together with our earlier data, these findings show that DR axons can stop by forming synaptic or dystrophic endings. They also suggest that dystrophic endings are formed at the borderline by occasional axons entrapped in collagen fibers, unlike synaptic endings that may be formed by many other axons making cellular contacts in deeper CNS territory well past the borderline.

Two-photon imaging confirms rapid immobilization of DR axons *in vivo*

In contrast to the prevailing view, these data suggest that only a few axons stop by forming dystrophic endings. The conventional view was primarily based on the observations that DRG axons *in vitro* retract in response to myelin-associated inhibitors (Li et al., 1996), or stall and become dystrophic when exposed to a gradient of CSPGs (Tom et al., 2004). Moreover, dystrophic endings remain extremely motile at least for several days (Cregg et al., 2014; Tom *et al.*, 2004). In contrast, DR axons that we monitored in living mice with widefield microscopy did not retract, but were rapidly immobilized as they entered the DREZ, where they remained

immobilized and the tips of only a few became noticeably enlarged (Di Maio *et al.*, 2011). To insure we have not overlooked subtle axon motility, we have now performed live imaging using high-resolution two-photon microscopy.

For optimal two-photon imaging, it is essential that fluorescent labeling mark only a small number of DR axons (Skuba et al., 2014). Accordingly, we used the M line of *Thy1* mice (Thy1-M), in which <5% of DRG neurons are YFP+ (Feng et al., 2000). Following DR crush, axons penetrate the crush site in a day or two, and then regenerate along the root at a speed of ~1 mm/day (Di Maio *et al.*, 2011). We crushed a L5 root >4 mm from the DREZ (Figure 2A), to make regenerating axons arrive at the DREZ as early as 5 days post-crush. We then screened ~150 mice on the first day of imaging at 4 or 5 dpi, to identify ~20 mice with 1 (or rarely 2) YFP+ axons superficially positioned within the optimum imaging depth (~150μm below the dura; Figure 2B). We then continuously monitored the distal endings of these axons for up to 5 hours. As anticipated, we observed axons at the DREZ at 5 dpi, but none at 4 dpi. Notably, no axons moved forward or retracted; all appeared already stopped at the DREZ. Axon tips with either a slender (Figure 2C) or small roundish shape (Figure 2D) exhibited no perceptible motility other than that due to respiration-induced artifacts. No axons that we monitored noticeably enlarged their tips. Following the first day of imaging, we imaged these axons repeatedly over several days to exclude the possibility that the immobility was due to phototoxicity (Figure S1). These findings indicate that most axons *in vivo* become rapidly immobilized, within a day or likely abruptly, by a stabilizing, rather than a repelling or collapsing, mechanism that was absent in *in vitro* studies. Considering that presynaptic differentiation is rapidly induced within one hour after target contact (Friedman et al., 2000; Lucido et al., 2009), they support further the notion that DR axons rapidly stop by making synaptic contacts.

OPCs are absent at the borderline; other glia are in locations unrelated to axon arrest

Immobilized axons formed synaptic contacts with non-neuronal cells (Di Maio *et al.*, 2011). To identify cellular element(s) that immobilize or stabilize axons, we next examined non-neuronal cells and their spatial relationship with axon arrest at the DREZ. At 2 wpi, axons that stopped past the borderline were not accompanied by Schwann cell processes (Figure 3A, 3C), showing

that they invaded CNS territory without leading, growth-supporting Schwann cells. These axons grew through CNS territory packed by astrocytes and oligodendrocytes, suggesting that these glia are unlikely to immobilize axons (Figure 3A, 3B, 3C). Macrophages were numerous peripherally but notably sparse in CNS territory (Figure 3B, 3C), indicating that the growth-collapsing activity of macrophages (Busch et al., 2009; Evans et al., 2014) is unlikely to be directly involved in the axon arrest. Blood vessels and pericytes, known for both growth-promoting and growth-inhibiting activity (Laredo et al., 2019; Partyka et al., 2019), were also sparse where many axons grew and stopped (Figure 3D).

Notably, when DRs were uninjured, OPCs and their processes were absent at and within ~50μm of the boundary, but abundant deeper in CNS territory (Figure 3D, 3E; Figure S2C). This distribution of resident OPCs was consistent in all mice (n >20) and was noteworthy because many axons grow across the borderline and then stop in deeper CNS territory (Zhai *et al.*, 2021). OPCs form functional synapses with neurons in adult brain (Bergles *et al.*, 2000; Mount *et al.*, 2019). Moreover, immobilized DR axons formed synaptic endings on non-neuronal cells that are not axons or astrocytes. They exhibited postsynaptic densities and presynaptic active zones that were noticeably thinner than at neuron-neuron synapses, and that resembled neuron-OPC synapses (Figure 1a: Di Maio *et al.*, 2011). Spatial analysis therefore distinguishes OPCs from other non-neuronal cells, raising the intriguing possibility that they are the postsynaptic cells stopping axons at the DREZ.

OPCs proliferate, migrate, and form a dense meshwork of processes after DR injury

Next, we examined responses of OPCs to DR injury in wholemounts, which permits comprehensive analysis of an entire root. We marked OPCs by immunolabeling NG2 proteoglycans and detected subsets of degenerating or regenerating YFP+ axons by using Thy1-H mice. In intact DRs, OPCs and their ramified processes were intraspinally distributed in a tile-like arrangement but were rare near the borderline (Figure S2A). At 2 wpi, many more OPCs formed a much denser meshwork of processes along the trajectory of degenerating distal axons (Figure S2B). OPC processes were now present near the borderline but remained relatively rare. Also notable was a highly upregulated expression of NG2 proteoglycans in the PNS (Figure S2B, S2C), presumably associated with Schwann cells (Tomita et al., 2019). Schwann cell-

associated NG2 staining in the PNS did not preclude identification of OPC processes, however, because it was tube-like and distinctly brighter than that associated with OPCs, which was highly ramified and directionless (Figure 4A). Temporal analysis in transverse sections showed that by 5 dpi, when DR axons stop at the DREZ, OPC processes migrated closer to the borderline, and by 2 wpi, they populated deeper CNS territory more densely (Figure S2C). OPCs also rapidly proliferated in response to the distant root injury; their proliferation peaked at 3 dpi, and their number doubled by 1 wpi (Figure S2D).

Stopped axons without dystrophic endings display extensive contacts with OPC processes

To determine if stopped axons are in association with OPCs, we next labeled regenerating axons with AAV2-GFP, and examined all detectable axon tips of entire roots in wholemounts at 2 wpi. Remarkably, distal ends of almost all, stopped axons were associated with a dense meshwork of OPC processes which made extensive contacts with axon endings and adjacent shafts (Figure 4A; n > 400 axons, 3 L5 DR). Transverse sections also showed that all axons that crossed the borderline and stopped in CNS territory were in direct contact with OPC processes (Figure 4B). Importantly, however, dystrophic endings observed at the borderline were not associated with OPCs (Figure 4B, Figure S3; n= >10). This finding is consistent with the absence of OPCs near the borderline (Figure 3D3) and the lack of cellular contacts by dystrophic endings (Figure 1B). These data suggest that some axons stop by forming dystrophic endings at the borderline where OPCs are absent, whereas others grow further and then stop by making extensive contacts with OPCs.

DR axons form synaptic endings on OPC processes

Next, we used immunolabeling for synaptic markers to determine whether axon-OPC contacts are synaptic. Consistent with the ultrastructural observation of aggregated synaptic vesicles (Figure 1A), a synaptic vesicle marker, SV2, brightly labeled small swellings of axon tips and shafts tightly associated with OPC processes, when assessed in wholemounts at 2 wpi (Figure 5A, 5B). However, SV2 and other vesicle markers also labeled dystrophic endings and axon swellings that showed no obvious OPC contacts. Other active zone and postsynaptic markers that we tested were also not convincingly selective (data not shown). Our attempts to trans-synaptically label OPCs by intra-DRG injections of pseudorabies or wheat-germ agglutinin

(WGA)-expressing viral tracers were unsuccessful. Other investigators have also failed to provide light microscopic identification of neuron-OPC synapses, an anatomically and functionally weaker synapse than neuron-neuron synapses (Bergles and Richardson, 2015; Kula et al., 2019).

To obtain more convincing evidence, we performed immuno-EM. At 2 wpi, we prepared longitudinal slices of dorsal spinal cord containing a DR and carefully examined the CNS and PNS areas across the borderline (Figure 5C). In the PNS, gold particles targeted to NG2 proteoglycans selectively labeled Schwann cells but not axons, confirming their specificity (Figure 5D). As anticipated, the immuno-EM procedures blurred the details of subcellular structures, making it difficult to readily identify apparent synaptic endings such as in Figure 1A. Nonetheless, we frequently observed presynaptic profiles that adequately indicated vesicle clustering and a thin postsynaptic density in direct apposition to gold particles-labeled OPC processes (Figure 5E). We also observed varicosity-like synaptic profiles, filled with numerous vesicles, formed on OPC processes that encircled the axons (Figure 5F). Notably, these postsynaptic processes were thinner than axons, and their membranes, but not cytoplasm, were labeled by gold particles, consistent with the transmembrane location of NG2 proteoglycan (Tamburini et al., 2019). Our immuno-EM therefore specifically identified OPCs as the postsynaptic cells that induced presynaptic differentiation of DR axons.

OPCs form functional synapses with co-cultured DRG neurons

Next, we co-cultured OPCs and DRG neurons to determine whether they form functional connections. As DR axons become unable to penetrate the DREZ, ~1 week after birth (Carlstedt et al., 1987; Golding et al., 1996), we purified OPCs from spinal cords of p16-P18 mice and co-cultured them with purified DRG neurons from adult mice. >95% pure OPCs at 3 div were labeled specifically by both markers of OPCs, NG2 and PDGFRα. They resembled OPCs *in vivo* by exhibiting a non-overlapping distribution of bushy NG2+ processes (Figure 6A). A few dissociated neurons were then applied sparsely to the cultured OPCs and co-cultured for 5 days in proliferating medium. The DRG neurons extended relatively short axons on OPCs, which continued to proliferate. Of note, DRG axons frequently developed small swellings which were

microtubule-deficient but SV2-enriched, a typical feature of presynaptic terminals (Figure 6Bb; arrows). We did not observe a large bulbous ending, reminiscent of *in vivo* dystrophic endings.

To determine whether these putative synaptic contacts were functional, we performed calcium imaging on the fifth day of co-culture. We loaded cultured cells with a fura-2 AM calcium indicator and located areas exhibiting OPC-axon contacts. We then locally infused 60mM KCL or 1mM glutamate to test if they selectively stimulated neurons. As anticipated, OPCs in our cultures were electrically active; rapid calcium responses were triggered not only from neurons but also from OPCs (data not shown). Therefore, to specifically stimulate neurons, we applied capsaicin, which selectively depolarizes nociceptive neurons by activating TRPV1 receptors (Szallasi and Blumberg, 1999). There were no spontaneous calcium responses in DRG neurons and OPCs (Figure 6C1). Local capsaicin infusion elicited rapid calcium responses in neurons, followed by calcium responses in adjacent OPCs (Figure 6C2). The responses in these OPCs were completely blocked by combined application of CNQX and AP5 (Figure 6C3), antagonists of AMPA/kainate and NMDA receptors known to be expressed in OPCs (Akay et al., 2021). Following washout of the antagonists, capsaicin-stimulation of the same neuron again evoked calcium responses in the same OPCs (Figure 6C4). These findings show that OPCs can form functional synapses with DRG neurons and reinforce the notion that axons rapidly stop regenerating by making extensive contacts with OPCs that induce presynaptic differentiation.

OPC ablation, although incomplete, enables many axons to regenerate into the spinal cord

Because no OPC-associated synaptogenic inducer has been identified, we could not selectively inhibit synapse formation between OPCs and DR axons. As an alternative, we genetically ablated OPCs to determine whether they halt DR axons reentering spinal cord. OPC ablation *in vivo* has been difficult because they are highly proliferative and subject to tight spatial homeostasis: residual OPCs vigorously repopulate a depleted area (Birey and Aguirre, 2015; Hughes et al., 2013). We therefore tried several transgenic strategies and diverse ablation paradigms. The best, yet incomplete, strategy was to use the PDGFRα-CreER driver and induce expression of diphtheria toxin subunit A (DTA). As DTA lacks the B subunit required for DT to penetrate membranes, ablation is strictly restricted to cells synthesizing DTA proteins, which elicit apoptotic extirpation (Brockschnieder et al., 2004). We crossed PDGFRα-CreER and

Rosa-DTA mice to generate PDGFRα-DTA mice and identified a 4-hydroxytamoxifen (4-HT) administration paradigm that elicited maximal ablation at 2 wpi (Figure 7A). Consistent with earlier studies that ablated OPCs by expressing DT receptors (DTR) (Birey et al., 2019; Djogo et al., 2016), PDGFRα-DTA mice looked normal, and western blotting revealed markedly reduced expression of NG2 and PDGFRα (Figure 7B). We also confirmed that ablation was selective for OPCs and did not evoke gross changes or pathologies in other cell types (Figure S4-S7). As anticipated, the extent of OPC ablation was quite variable, ranging between 20-80% at 2 wpi, as determined by mean fluorescence intensity of NG2 in the spinal cord. None of the administration regimens that we tried achieved more consistent or complete ablation around 5 dpi. We therefore selected mice with at least 60% ablation at 2 wpi for further analysis (Figure 7C).

At 2 wpi, some OPC processes usually remained at the DREZ even in mice with ~80% ablation of OPCs (Figure 7D, Figure S4A), presumably reflecting more vigorous proliferation of OPCs along the trajectory of degenerating old axons. Remarkably, despite residual and repopulating OPCs, PDGFRα-DTA mice showed a greater number of axons at and beyond the DREZ (i.e., 100μm of the borderline) than control mice (Figure 7D). The number of axons counted peripherally in PDGFRα-DTA mice did not differ from that in control mice, indicating that the enhanced regrowth was not due to an increase in axons regenerating peripherally (Figure 7E). Quantification of GFP+ axons showed that OPC ablation almost tripled the number of axons that extended past the DREZ (Figure 7F). Several considerations make the increase even more noteworthy. First, axons frequently extended unusually deeply, into the dorsal funiculus (Figure 7D2’’; arrow). Second, AAV2-transduced GFP+ axons are predominantly large-diameter axons whose growth capacity is particularly weak (Zhai *et al.*, 2021), yet even incomplete OPC ablation enabled ~30% of these weak regenerators to cross the DREZ. Indeed, such a large increase rivaled the levels achieved by combining a conditioning lesion with simultaneous removal of myelin inhibitors and CSPGs (Zhai *et al.*, 2021).

Enhanced regeneration is not due to indirect effects of OPC ablation

Apoptosis does not induce an inflammatory response (Labbé and Saleh, 2008; Weinrauch and Zychlinsky, 1999). Furthermore, consistent with earlier studies of OPC ablation (Birey *et al.*, 2019; Liu and Aguzzi, 2020; Xiao et al., 2022), the inflammatory responses of PDGFRα-DTA

mice were comparable to those of control mice (Figure S5): the morphology, distribution, and numbers of microglia and macrophages in the spinal cord and DRs were not significantly different. Astrocytes, which inhibit Schwann cell migration (Afshari et al., 2010), also showed no differences in morphology, density, or reactivity (Figure S6). NG2 staining in the PNS of PDGFRα-DTA mice was slightly diminished, as compared to control mice, at 2 wpi (Figure S4B, S4C). Because Schwann cells modestly express PDGFRα mRNA (Gerber et al., 2021), they might be directly impacted in PDGFRα-DTA mice. However, the density and reactivity of Schwann cells in PDGFRα-DTA and control mice were not significantly different (Figure S7). Moreover, similar numbers of axons extended from the PNS (Figure 7E), additionally indicating that Schwann cells were minimally if at all affected and that they did not significantly attenuate regeneration. Lastly, NG2, also known as CSPG4, is a constituent of growth inhibiting CSPGs (Tran et al., 2018; Varadarajan *et al.*, 2022). It is conceivable, therefore, that a reduction of NG2/CSPG4 is the basis of enhanced regeneration by OPC deletion. We found, however, abundant expression of CSPGs in PDGFRα-DTA mice, as indicated by CS56 immunoreactivity, associated with other cell types expressing CSPGs, including astrocytes, macrophages, pericytes, and residual OPCs (Figure S4C). Moreover, we were unable to achieve more robust regeneration even after broad removal of all CSPGs (Zhai *et al.*, 2021). Collectively, these data exclude that the enhanced regeneration was due to indirect effects on axons by ablating OPCs.

Axons continue regenerating intraspinally through areas lacking OPCs

Axon endings remained remarkably stable at the DREZ for at least 4 months after injury (Di Maio *et al.*, 2011). We also reported that most axons still stop and remain immobilized for at least 4 weeks after injury, despite simultaneous and prolonged removal of myelin inhibitors and CSPGs (Zhai *et al.*, 2021). If OPCs play a primary role in stopping axons, then axons may continue to grow with prolonged ablation of OPCs, even in the presence of major growth inhibitors. To test this notion, we examined PDGFRα-DTA mice after longer survival, 4 wpi (Figure 8A). As anticipated, OPCs widely repopulated and re-formed an OPC meshwork in most areas of the spinal cord in these mice; their overall densities corresponded to ~70% of those in control mice (Figure 8B). Of note, OPC repopulation was not uniform; there were areas in which OPCs remained reduced or sparse (Figure 8D, S8).

Consistent with our previous study, in control mice, regeneration across the DREZ did not increase between 2 wpi and 4 wpi (Figure 8D, 8E). In striking contrast, in PDGFRα-DTA mice, GFP+ axons more frequently extended significantly deeper into the dorsal funiculus at 4 wpi than at 2 wpi (Figure 8D, S8) and occasional axons regrew remarkably deeply into the dorsal horn (Figure 8D). Intraspinal growth of DR axons that reached deep layers of the dorsal horn was indeed extraordinary, because it was not achieved even by a nerve conditioning lesion or PTEN deletion (Zhai *et al.*, 2021; Kim et al in preparation). Also notable was a conspicuous reduction of OPCs in areas where more axons grew deeper (Figure 8D). Furthermore, axons that extended through OPC-deficient areas terminated in OPC-rich regions, making extensive contacts with OPC processes (Figure S8). The number of axons extended from the PNS did not increase (Figure 8C) nor did the number of axons counted at 100μm from the borderline in the CNS (Figure 8E). Therefore, the enhanced regeneration was due to sustained growth of the axons already present at the DREZ at 2 wpi, rather than by axons that freshly crossed the borderline. Taken together, these findings indicate that axons continued to regenerate deep into the spinal cord until they encountered residual or repopulating OPCs.

DISCUSSION

Here, we newly elucidated a major role of OPCs in arresting sensory axons regenerating into the spinal cord. Together with additional insights into dystrophic endings and other glia, we propose a new model for the regeneration failure at the DREZ (Figure 8F): Regenerating axons exiting basal lamina tubes at the borderline turn around, or stop immediately by forming dystrophic endings if their growth is obstructed by fibrous collagens. Most axons, however, cross the borderline into CNS territory, albeit extending slowly due to poor regenerative ability, extrinsic growth-inhibitory molecules (myelin-inhibitors and CSPGs etc.), and lack of leading Schwann cells. These axons soon stop as they encounter a dense meshwork of OPC processes that induce presynaptic differentiation. Concurrent induction at numerous contacts results in rapid and persistent synaptic stabilization.

Our findings definitively demonstrate that DR axons stop in two distinct ways, forming dystrophic or synaptic endings. The large bulbous endings that we observed at the border may not represent the only type of dystrophic endings (Hill, 2017). It is noteworthy that our EM

studies have frequently revealed synapses or synapse-like profiles, but no apparent dystrophic endings, in the CNS beyond the borderline. Other investigators also observed synapse-like endings (termed synaptoids) and postulated the presence of "physiological stop signals" arresting DR axons (Carlstedt, 1985; Liuzzi and Lasek, 1987). We suggest, therefore, that dystrophic endings form exclusively at the border area where OPCs are sparse, by occasional axons obstructed by collagen matrix. Bolstering this notion is that intraneural fibrosis following traumatic injury or demyelination, extracellularly accumulating fibrous collagens that can impede axon regeneration (Dorrier et al., 2021; Soderblom et al., 2013). Considering the much slower axon degeneration and weaker inflammatory responses in the CNS than PNS (Vargas and Barres, 2007), the extent of intraneural fibrosis or collagen accumulation is likely higher at the border and peripherally along the root (Vargas and Barres, 2007). Interestingly, extensive fibrosis inhibits OPC migration (Dorrier *et al.*, 2021), suggesting that fibrous collagens may trap dystrophic endings and repel OPCs from the border area.

Our data are the first demonstration that OPCs stop regenerating axons, and that they do so by inducing synaptic differentiation. Silver's group reported the seemingly analogous finding that spinal cord axons dying-back after injury stop degenerating by initially making synaptic-like contacts with NG2+ cells and then forming dystrophic endings (Filous et al., 2014). NG2/CSPG4 mediated the purportedly synaptic entrapment, because knockout mice globally lacking NG2/CSPG4 showed reduced entrapment, lengthened dying-back, and a net positive impact on spinal cord regeneration (Filous *et al.*, 2014). Notably, however, synapses with apparent ultrastructural features were not observed (Jerry Silver, personal communication). OPC-neuron synapses readily formed in the absence of NG2/CSPG4 (Passlick et al., 2016). Additionally considering that the study examined degenerating, not regenerating, axons, we posit that NG2/CSPG4-mediated stabilization of dying-back axons is not identical to OPC-mediated synaptic arrest of regenerating axons. It remains to be determined if spinal cord axons stop regenerating by forming synapses with OPCs.

Approximately 70% axons did not turn around or stop at the borderline, but invaded CNS territory. This is surprising considering the limited ability of axons to cross astrocyte-Schwann cell interfaces (Warren et al., 2020; Wiliams and Bunge, 2012). However, axons can use bridges

formed by astrocytes to cross the DREZ (Li et al., 2004) and spinal cord lesions (Zukor et al., 2013). Astrocytic processes invade peripherally after DR injury and are frequent within Schwann cell basal lamina tubes (Fraher, 2002). We suggest, therefore, that astrocytic guidance is initiated peripherally and that it enables many axons to cross the borderline.

When these ~70% axons are immobilized, a dense meshwork of OPC processes forms at the DREZ, and that these processes make extensive contacts with axon tips and shafts. Furthermore, their contacts are apparently synaptic; 1) OPC-axon contacts are intensely co-labeled by synaptic markers; 2) OPCs are ultrastructurally postsynaptic, displaying features of OPC-neuron synapses; 3) OPCs form functional synapses with adult DRG neurons. Remarkably, OPC depletion prolongs axon regeneration beyond the borderline apparently by sustaining intraspinal axon growth. These data, together with our earlier findings, strongly suggest that OPCs play a primary role in arresting axons by inducing presynaptic differentiation. Consistent with our conclusion, DRG neurons downregulate presynaptic proteins essential for synaptic transmission, such as $\alpha_2\delta$ calcium channel subunits, as they regain the ability to grow their axons (Tedeschi et al., 2016). Furthermore, genetic or pharmacological targeting of $\alpha_2\delta$ or another active zone protein, Munc13, promotes regeneration of dorsal column axons after spinal cord injury (Hilton et al., 2022; Tedeschi *et al.*, 2016). Intact axon branches maintaining synaptic connections similarly suppress regeneration of injured axon branches (Lorenzana et al., 2015).

How OPCs induce presynaptic differentiation remains speculative. OPCs express several synaptogenic molecules, including Nlgn1-3 (Neuroligin1-3), Cadm1a/1b (SynCAM1a/1b), Lrrc4 (NGL-3), and Lrrtm 1/2 (Hughes and Appel, 2019). Neuroligin and SynCAM are transsynaptic adhesion molecules that trigger presynaptic assembly when expressed in non-neuronal cells (Pinto and Almeida, 2016; Südhof, 2018). Also undetermined is whether the formation of OPC-DR axon synapses requires synaptic transmission or activity. Notably, inhibition of synaptic transmission promoted regeneration of DC axons (Hilton *et al.*, 2022; Tedeschi *et al.*, 2016), whereas stimulation of synaptic transmission promoted regeneration of DR axons (Wu et al., 2020). Although neuron-neuron synaptogenesis *per se* proceeds in the absence of neuronal activity (Held et al., 2020; Verhage et al., 2000), activity levels may have a differential effect on synapse number and maturation in different contexts (Andreae and Burrone, 2014). It will,

therefore, be interesting to determine how activity levels of DRG neurons affect OPC-mediated synaptic arrest of DR axons.

To verify the dominant role of OPCs, we sought to determine whether a nerve conditioning lesion would dramatically enhance regeneration if OPCs are depleted. However, the efficiency of OPC deletion was reduced further by a conditioning lesion, and we were unable to obtain conclusive results (data not shown). Attempts to survey the mobility of axons arriving at the DREZ were also unsuccessful, because too many OPCs remained at 5 dpi. It is worth emphasizing, therefore, that we observed noticeably enhanced regeneration despite the continued presence of ~30% OPCs at 2 wpi and ~70% OPCs at 4 wpi. We anticipate that more complete depletion of OPCs and/or selective targeting of OPC-neuron synapses will enable far more axons to continue regenerating more deeply into the spinal cord. Lastly, the ability of OPCs to differentiate into myelinating oligodendrocytes is limited, although a surplus number are rapidly generated after demyelination (Skaper, 2019). The function of OPC-neuron synapses also remains enigmatic (Akay *et al.*, 2021). Future efforts to determine if OPCs elsewhere in the CNS curtail axon plasticity and/or regeneration, may have significant basic science and clinical implications.

ACKNOWLEDGMENTS

We thank Drs. Alan Tessler, Tim Himes, George Smith, and Gareth Thomas for critical reading of the manuscript. We thank Dr. Dwight Bergels for guinea pig anti-NG2 antibody, Drs. Dewight Williams and Biao Zuo at the Penn Electron Microscopy Resource Laboratory for technical support for TEM and immunoEM. We sincerely thank Dr. Ahmet Hoke for motivating the study, Drs. Jerry Silver and Theresa Connors for earlier immunoEM efforts, Dr. Michael Lane for pseudorabies virus, Dr. Jian Zhong for WGA-transsynaptic virus and Dr. George Smith for AAV2-GFP. This work was supported by grants from NIH R01 (NS079631) and Shriners Children's to Y-J Son. H.K. was a recipient of Craig H Neilson postdoctoral fellowship (280274).

AUTHOR CONTRIBUTIONS

Conceptualization, Y-J.S.; methodology, S.K., H.H.; investigation, H.K., A.S., J.X., S.H., J.Z., R.Y., Y-J.S.; writing—original draft, H.K.; writing—review and editing, Y-J.S.; funding acquisition, Y-J.S.; resources, S.K.,; supervision, Y-J.S.

COMPETING INTERESTS

The authors declare no competing interests.

FIGURE LEGENDS

Figure 1. Dystrophic endings form by axons embedded in collagens at the borderline

(A, B) Ultrastructural comparison of a synaptic ending (A) and a dystrophic ending (B), with corresponding enlarged views (a, b), formed by DR axons (Green) at the DREZ at 2 wpi. The presynaptic ending is small, organized, and apposed to an unknown postsynaptic cell (Red; a), whereas the dystrophic ending is large, disorganized, and embedded in acellular collagen fibers (B, b). Scale bar: 500nm

(C-C3) The incidence and location of dystrophic endings analyzed on transverse sections, at 2 weeks after C5-C8 root crush followed by AAV2-GFP injections to C5 and C7 DRGs (C). A representative section (C1), with enlarged view (c), showing a large dystrophic ending (asterisk) formed at the borderline (dotted line). Note that many other axons stopped past the borderline do not display dystrophic endings. Representative quantification of a mouse showing the incidence of dystrophic endings (C2) and their location relative to the borderline (C3) (n=191 axons, >15 serial sections). Scale bar: 20μm

(D-D2) High resolution 3D imaging and quantitative analysis of different axon endings on wholemounts of CLARITY cleared spinal cords at 2 weeks after L4 and L5 root crush (D). Transmitted light (D1) and fluorescent (D1', d, d') views of a representative cleared spinal cord, roots, DRG (inset in D1'), and GFP+ axons arrested at the DREZ in enlarged (d) or volume rendered images (d'). Representative examples illustrate parental axons that turn around (e.g., d'-1), form a large dystrophic ending (e.g., d'-2), or form a small putative synaptic ending (e.g., d'-3). Relative incidence of different axon endings illustrating that a limited number of parental axons turned around or stopped by forming dystrophic endings (D2). n= >100 axons/mouse, 3 mice. Scale bars: 200μm (D1, D1'), 50μm (D1', inset), 50μm (d, d'), 10μm (d'1-3)

Figure 2. Two-photon imaging confirms rapid axon immobilization at the DREZ

(A) Schematic illustration of the experimental procedure for two-photon imaging of DR axons in live Thy1-YFPM mice after L5 root crush.

(B) A widefield view of the DREZ area, taken at 5 dpi, showing an axon of interest (arrows) and fluorescent debris of degenerating old axons and a midline vein that served as landmarks (asterisks). Subsequent imaging sessions of this axon are shown in **Figure S1**. Scale bar:100μm

(C, D) Two-photon imaging of representative axon tips with either slender (C) or small roundish shape (D), taken every 30 min on 5 dpi. Arrows denote immobile axon tips and asterisks denote landmarks. Scale bar: 50μm (C, D), 20μm (D, insets)

Related data are available in **Figure S1**.

Figure S1. Daily *in vivo* monitoring of the same axons following two-photon imaging

Widefield *in vivo* images of the same axon taken daily after two-photon imaging on 4 or 5 dpi, illustrating that the axon tip (arrows) does not degenerate, excluding that immobility is due to phototoxicity. Asterisks denote axon debris and branching points of blood vessels that served as landmarks. Scale bar: 1mm

Figure 3. OPCs are absent at the borderline; the location of other glia is unrelated to axon arrest

(A, B) Transverse sections of a spinal cord 2 weeks after cervical root crush followed by intraganglionic injection of AAV2-GFP.

(A) A DREZ area illustrating spatial relationships of arrested GFP+ axons (A2) with GFAP-labeled astrocytes (A1) and p75-labeled Schwann cell processes (A3). Many axons extend across the borderline (dotted line) by growing through astrocytic processes without association with leading Schwann cell processes. Scale bar: 50μm

(B) A DREZ area illustrating spatial relationships of arrested axons (refer to A2) with MOG-labeled oligodendrocytes (B1), SC2E-labeled myelinating Schwann cells (B2), and ED1-labeled macrophages (B3). Macrophages are enriched peripherally but sparse at the DREZ. Scale bar: 50μm

(C) Diagram summarizing insignificant spatial relationships of arrested axons with oligodendrocytes, astrocytes, Schwann cells, and macrophages at axotomized DREZ.

(D) A DREZ area of uninjured DRs illustrating that NG2-labeled OPCs (D3) are absent at and immediately near the borderline (dotted line), denoted by astrocytes (D1) and oligodendrocytes (D2), but abundant deeper in CNS territory (>50μm from the borderline). Arrow in D3 denotes NG2-labeled pericytes associated with a blood vessel. Scale bar: 50μm

(E) Diagram illustrating the distance and position of OPC processes relative to the borderline (dotted line) at intact DREZ with no axon injury.

Related data are available in **Figure S2**.

Figure S2. OPCs proliferate, migrate, and form a dense meshwork of processes after DR injury

(A, B) Wholemount views of intact (A) and axotomized (B) DREZ area showing subsets of YFP+ axons (A, B) and the distribution of NG2-labeled OPCs and their processes (A', B'). Dotted line approximates the borderline (dotted line) denoted by GFAP-labeled astrocytes (A", B"). Enlarged images (a', b') show area near the borderline (asterisks) and deeper in CNS territory. Scale bar: 100μm

(C) Transverse sections of intact (C1, C1') or axotomized DREZ at 5 dpi (C2, C2') and 2 wpi (C3, C3'), co-labeled for NG2 (C1-C3) and GFAP (C1'-C3'), illustrating temporal development of a dense meshwork of OPC processes populating the DREZ after DR injury. Scale bar: 50μm

(D) Quantification of OPC proliferation by counting nuclei colabeled by Olig2, a marker of OPCs and oligodendrocytes (D1), and Ki67, a marker of cell proliferation (D2), illustrating rapid proliferation of OPCs after DR injury that peaks at 3 dpi (D3) and doubles the number of Olig2+ cells by 1 wpi (D4). N= >3 sections/each mouse, 5 mice/each time point. Error bars represent SEM. p values are calculated by one-way repeated measures ANOVA with Tukey's post hoc test. ns, $p > 0.05$; *$p \leq 0.01$, **$p \leq 0.001$, ***$p \leq 0.0001$.

Figure 4. Stopped axons without dystrophic endings display extensive contacts with OPC processes

(A) Wholemount views of the DREZ area in low (A-A'") and high (a1-a2'") magnifications at 2 wpi, showing GFP+ axons (A, a1, a2), NG2-labeled OPCs (A', a1', a2'), and p75-labeled Schwann cells (A", a1", a2"). Arrows in enlarged views (a1-a2'") indicate examples of direct

contact points between OPC processes and arrested axons. NG2 staining in the PNS is intense after DR injury but does not preclude identification of OPC processes. Scale bar: 100μm

(B) Transverse sections in low (B-B") and high (b-b") magnifications showing GFP+ axons (B, b) and NG2-labeled OPCs (B, b) at 2 wpi. Arrowheads indicate an example of many axons that stopped past the borderline (dotted line) in association with OPC processes. Arrows indicate a dystrophic ending formed at the borderline that, in contrast, lacks contacts with OPC processes. Scale bar: 50μm

Related data are available in **Figure S3**.

Figure S3. Dystrophic endings lack direct contacts with OPC processes

(A, B) Two transverse sections at 2 wpi, showing large bulbous endings (arrows) formed by some GFP+ axons (A, B) at the borderline (dotted line), NG2-labeled OPCs (A', B'), and GFAP-labeled astrocytes (A", B"). These putative dystrophic endings form where OPC processes are rare. Scale bar: 50μm.

Figure 5. DR axons form synaptic endings on OPC processes

(A) Wholemount views of the DREZ area at 2 wpi in low (A) and high magnifications (a-a'''), showing GFP-labeled axons (a), SV2-labeled synaptic vesicles (a'), and NG2-labeled OPCs (a"). Boxed area in A shows several axons with small swellings on axon tips and shafts (a) intensely labeled for SV2 (a') and tightly associated with OPC processes (a"). Asterisks indicate same positions in a-a'''. Scale bar: 100μm (A), 50μm (a-a''')

(B) Volume rendered image (b) of a boxed area in B, illustrating direct contacts of axon swellings (Green) with OPC processes (Red). Scale bar: 5μm

(C) Diagram showing procedures to prepare a longitudinal vibratome slice of dorsal spinal cord with attached DR at 2 wpi.

(D) An electron micrograph of the PNS area showing gold particles (arrows) targeted to NG2 selectively labeling Schwann cells (SC). Scale bar: 500 nm

(E) An area of the DREZ showing that OPC processes denoted by gold particles (arrows) form synaptic contacts with axons. Magnified view of boxed area (e) illustrates synaptic contacts (asterisks) with presynaptic clustering of synaptic vesicles and thin postsynaptic density. Scale bar: 100 nm (E, e)

(F) An electron micrograph illustrating varicosity-like synaptic profile formed by DR axon encircled by OPC processes identified by gold particles (arrows). Scale bar: 100 nm

Figure 6. OPCs form functional synapses with co-cultured DRG neurons

(A) >95% pure OPCs, cultured from spinal cords of p16-18 mice, immunolabeled at 3 div for DAPI (A), Olig2 (A') and NG2 (A"), and PDGFRα (A'"). Enlarged view (a") of boxed area in A" illustrates OPCs with bushy processes resembling OPCs *in vivo*. Scale bar: 20μm

(B) Purified OPCs and DRG neurons co-cultured for 5 days, showing DAPI (B), NG2-labeled OPCs (B'), Tuj1-labeled axons (B"), and SV2-labeled synaptic vesicles (B'"). Magnified view (b'") of boxed area in B'" illustrates microtubule-deficient but SV2-enriched axonal swellings (arrows) formed on OPCs. Scale bar: 50μm

(C) Representative calcium imaging recordings of OPC-DRG neurons co-cultured for 5 days, illustrating temporal calcium responses of a neuron (red arrows) and two adjacent OPCs (black arrows), before (C1) and following capsaicin stimulation of neurons without (C2) or with antagonists of AMPA/kainate and NMDA receptors (C3), CNQX and AP5. Following washout of antagonists (C4), capsaicin stimulation of the same neuron again elicits calcium responses in the same OPCs. Scale bar: 30μm

Figure 7. Genetic OPC ablation, although incomplete, markedly enhances axon regeneration

(A) Diagram illustrating experimental procedures to evaluate the effects of genetic OPC ablation at 2 weeks after C5-C8 root crush followed by AAV2-GFP injections to C5 and C7 DRGs.

(B) Western blotting showing markedly reduced markers of OPCs, NG2, and PDGFRα, in PDGFRα-DTA mice.

(C) Quantitative comparisons of OPC density measured by mean fluorescence intensity of NG2 staining in the spinal cord, illustrating ~70% ablation of OPCs in PDGFRα-DTA mice used for the analysis. Error bars represent SD. Unpaired t test (n=5 control, 6 DTA mice). ****$p \leq 0.00001$

(D) Transverse sections of a control (D1-D1'") and a PDGFRα-DTA mouse with ~80% OPC ablation (D2-D2'") at 2 wpi showing GFAP-labeled astrocytes (D1, D2), NG2-labeled OPCs (D1', D2'), and GFP+ axons (D1'", D2'"). Enlarged views of boxed area (d1'", 1, 2) illustrate that

more axons cross the border and DREZ in the PDGFRα-DTA mouse. Blue lines approximate ~100μm wide region of the DREZ. Dotted lines denote borderline identified by GFAP staining. Insets in D1' and D2' are magnified views of the DREZ, illustrating residual and/or repopulating OPCs in PDGFRα-DTA mice. An arrow in D2" denotes axons extending unusually deeply into the dorsal funiculus. Scale bar: 100μm (D1-D2'''), 50μm (d1''', 1, 2)

(E) Quantification of GFP+ axons at ~100μm proximal to the borderline in the PNS, illustrating insignificant difference between control and PDGFRα-DTA mice. Error bars represent SEM (n = 4 mice/group). Unpaired Student's t-test. ns, $p > 0.05$

(F) Quantitative comparisons of control and PDGFRα-DTA mice illustrating that OPC ablation, although incomplete, triples the number of axons extending past the DREZ. Error bars represent SEM (n=4 mice/group). Two-way repeated-measures ANOVA with Tukey's multiple comparisons test. 100μm, ****$p \leq 0.00001$; 200μm, ns, $p > 0.05$; 300μm

Related data are available in **Figure S4-S7**.

Figure S4. Comparison of NG2/CSPG4 and CSPGs expression in control and PDGFRα-DTA mice

(A) Transverse sections of a control (A1) and a PDGFRα-DTA mouse with ~80% OPCs ablated at 2 wpi (A2), co-labeled for NG2 (a1, a2) and GFAP (a1', a2'), illustrating a marked reduction in OPCs and their processes in the spinal cord of the PDGFRα-DTA mouse. Enlarged views of the boxed area in A1 and A2 show slightly reduced NG2 immunostaining peripherally along the DR of the PDGFRα-DTA mouse (a2), as compared to control mouse (a1). Scale bar: 100μm

(B) Quantitative comparisons of control and PDGFRα-DTA mice, illustrating a slight reduction of NG2 immunoreactivity in dorsal roots of DTA mice. Unpaired Student's-t test (n=5 control, 6 DTA mice). Error bars represent SEM. *$p \leq 0.01$

(C) Transverse sections of a control (C1-C1") and a PDGFRα-DTA mouse (C2-C2"), co-labeled for NG2 (C1, C2) and for CS56 (C1', C2') at 2 wpi, showing reduced NG2 but abundant CSPGs associated with the DREZ area of DTA mice. Scale bar: 100μm

(D) Quantitative comparisons of control and PDGFRα-DTA mice, illustrating insignificant difference in CS56 immunoreactivity measured in the dorsolateral funiculus including the

DREZ. Unpaired Student's t-test (n=2 control, 3 DTA mice). Error bars represent SEM. ns, $p > 0.05$

Figure S5. Comparison of microglia and macrophages in control and PDGFRα-DTA mice

(A) Transverse sections of a control (A1-A1''', A3 and A3') and a PDGFRα-DTA (A2-A2''', A4 and A4') mouse at 2 wpi, showing DAPI, NG2-labeled OPCs, and Iba1-labeled microglia, and illustrating no noticeable differences in morphology or density of microglia in the spinal cord, DREZ, or DR of control and DTA mice. Scale bar: 500μm

(B) Transverse sections from a control (B1-B1''', B3 and B3') and PDGFRα-DTA (B2-B2''', B4 and B4') mouse at 2 wpi, showing DAPI, NG2-labeled OPCs, and ED1-labeled macrophages, and illustrating no noticeable differences in the distribution or density of macrophages in the spinal cord, DREZ, or DR of control and DTA mice. Scale bar: 500μm

(C) Quantitative comparisons of control and PDGFRα-DTA mice illustrating insignificant difference in the number of Iba1+ microglia in the spinal cord. Unpaired Student's t-test (n=3 mice/group). Error bars represent SEM. ns, $p > 0.05$

(D, E) Quantitative comparisons of control and PDGFRα-DTA mice, illustrating insignificant difference in the number of ED1+ macrophages in the spinal cord (D) or dorsal root (E). Unpaired Student's t-test (n=3 mice/group). Error bars represent SEM. ns, $p > 0.05$

Figure S6. Comparison of astrocytes in control and PDGFRα-DTA mice

(A) Transverse sections of control (A1-a1''') and PDGFRα-DTA (A2-a2''') mice at 2 wpi, co-labeled for NG2 and GFAP, illustrating no noticeable differences in the density or distribution of astrocytes at the DREZ or within the spinal cord between control and DTA mice. Scale bar: 500μm

(B) Quantitative comparisons of control and PDGFRα-DTA mice, illustrating insignificant difference in the number of ED1+ macrophages in the spinal cord. Unpaired Student's t-test (n=3 mice/group). Error bars represent SEM. ns, $p > 0.05$

Figure S7. Comparison of Schwann cells in control and PDGFRα-DTA mice

(A) Transverse sections of control (A1-A1'") and PDGFRα-DTA (A2-A2'") mice at 2 wpi, illustrating that p75 immunoreactivity in dorsal root of DTA mouse is comparable to that of control mouse. Scale bar: 500μm

(B) Transverse sections of control (B1-B1'"") and PDGFRα-DTA (B2-B2'"") mice at 2 wpi, illustrating no noticeable difference in the number of Sox10-labeled Schwann cells present in the dorsal root. Scale bar: 100μm

(C) Quantitative comparison of control and PDGFRα-DTA mice, illustrating insignificant difference in p75 immunoreactivity in the dorsal root. Unpaired Student's t-test (n=3 mice/group). Error bars represent SEM. ns, $p > 0.05$

(D) Quantitative comparison of control and PDGFRα-DTA mice, illustrating insignificant difference in the number of Schwann cells in the dorsal root. Unpaired Student's t-test (n= 4 control, 5 DTA mice). Error bars represent SEM. ns, $p > 0.05$

Figure 8. Axons continue regenerating intraspinally through areas lacking OPCs

(A) Diagram illustrating experimental procedures to evaluate the effects of genetic OPC ablation at 4 weeks after C5-C8 root crush followed by AAV2-GFP injections into C5 and C7 DRGs.

(B) Quantitative comparison of OPC density, measured by mean fluorescence intensity of NG2 staining in the spinal cord, illustrating ~30% ablation of OPCs in PDGFRα-DTA mice used for the analysis. Error bars represent SD. Unpaired t test (n=4 control, 5 DTA mice). ns, $p > 0.05$

(C) Quantification of GFP+ axons at ~100μm proximal to the borderline, illustrating insignificant difference between control and PDGFRα-DTA mice. Error bars represent SEM (n = 4 mice/group). Unpaired Student's t-test. ns, $p > 0.05$

(D) Transverse sections from a control (D1-D1'") and a PDGFRα-DTA mouse (D2-D2'"), illustrating massive repopulation of OPCs (D2') and GFP+ axons that regenerate remarkably deeply into the dorsal horn (D2"; arrows). There are noticeably fewer OPC processes where more axons (arrowheads) regrow within the spinal cord (area 1 in D2') than where fewer axons (arrows) regenerate (area 2 in D2"). Enlarged view of boxed area in D2" illustrates regenerated GFP+ axons in association with repopulated OPC meshwork (d2). Scale bar: 100μm

(E) Quantitative comparison of control and PDGFRα-DTA mice illustrating that ~20% axons continue to regenerate past the DREZ in DTA mice during the additional two weeks. The

number of axons counted at 100μm past the borderline remains unchanged at 4 wpi in DTA mice. Error bars represent SEM (n=4 mice/group). Two-way ANOVA with Sidak's multiple comparisons test. 100μm; ns, $p > 0.05$ (DTA 4 wpi vs. DTA 2 wpi); ****$p \leq 0.00001$ (DTA 4 wpi vs. control 4 wpi), 200μm; ****$p \leq 0.00001$ (DTA 4 wpi vs. control 4 wpi), *$p \leq 0.01$ (DTA 4 wpi vs. DTA 2 wpi), 300μm; ns, $p > 0.05$ (DTA 4 wpi vs. control 4 wpi, DTA 2 wpi).
(F) Schematic illustration of the proposed model of how DR axons terminate regenerating at the DREZ, highlighting OPCs as a major regenerative barrier.
Related data are available in **Figure S8**.

Figure S8. **Axons regenerate deeper into the dorsal funiculus in PDGFRα-DTA mice at 4 wpi**
(A1-A1''', A2-A2''') Two sets of transverse sections of PDGFRα-DTA mice at 4 wpi, co-labeled for GFAP and NG2, illustrating more numerous GFP+ axons (A1", A2") that regenerated deeper into the dorsal funiculus than at 2 wpi (refer to Figure 7D2"). These axons terminate where OPCs are locally repopulated, in association with OPC processes (A1', A2'). Enlarged views of boxed area (a1-a2'") also indicate sparse distribution of OPCs where these axons regenerate. Arrows in A2" show axons reaching more deeply into the dorsal horn. Scale bar: 50μm

METHODS

Mice

All animal care and procedures were conducted in accordance with the National Institute of Health guidelines and with approval from the Institutional Animal Care and Use Committee at Lewis Katz School of Medicine at Temple University. For *in vivo* imaging or CLARITY tissue clearing, C57BL/6J or the transgenic strains, *Tg(Thy1-EGFP)MJrs/J* (Thy1-GFP-M; JAX 007788) or *B6.Cg-Tg(Thy1-YFP)HJrs* (Thy1-YFP-H; JAX 003782) were purchased from Jackson Laboratory. For OPC ablation, *B6N.Cg-Tg(Pdgfra-cre/ERT)467Dbe/J* (PDGFRα-creER^{TM}; JAX 018280) and *B6.129P2-Gt(ROSA)26Sortm1(DTA)Lky/J* (Rosa26-DTa; JAX 009669) purchased from Jackson Laboratory were crossed to generate *PDGFRα-creER^{TM}; Rosa26-DTa* mice. Adult mice of either sex, 2-3 months old, were used for all experiments. Age-matched *PDGFRα-creER^{TM}* or *Rosa26-DTa* mice were used as the control.

Dorsal root crush

For unilateral cervical (C5-C8) or lumbar (L4 and L5) root crush, mice were anesthetized with an intraperitoneal injection of xylazine (8 mg/kg) and ketamine (120 mg/kg). Following a 2- to 3-cm-long incision in the skin of the back, the spinal musculature was reflected and the C5-C8 or L3–S1 spinal cord segments exposed by hemilaminectomies. A small incision was made in the dura overlying each targeted DR. A fine forceps (Dumont #5; Fine Science Tools, Foster City, CA) was introduced subdurally and each DR was crushed for 10 s. To avoid scar formation and possible compression, we applied a piece of thin silastic membrane (Biobrane, Bertek Pharmaceuticals, Sugarland, TX) over the hemilaminectomy site and covered it with a layer of thicker artificial dura (Gore Preclude MVP Dura Substitute, W.L. Gore and Associates, Flagstaff, AZ). The overlying musculature was closed with 5-0 sutures, and the skin closed with wound clips. All animals received subcutaneous injections of saline (0.9% w/v NaCl) and buprenorphine (0.05 mg/kg) for postoperative pain management.

Intraganglionic injection of AAV2-GFP

Recombinant adeno-associated virus 2 carrying eGFP (AAV2-GFP) with CMV-enhanced chicken β-actin (CAG) promoter was purchased from Vector Biolabs (Malvern, PA; stock #7072) or generated as previously described (Liu et al., 2014). AAV2-GFP was microinjected into a DRG using a micropipette pulled to a diameter of 0.05 mm and a nanoinjector (B203XVY Nanoliter 2000; World Precision Instruments, Sarasota, FL). For each injection, the micropipette was introduced 0.5 mm into the DRG and a total volume of AAV (1 μl/DRG) containing >1 X 10^{13} GC/ml injected over a 10 min period. The glass needle was left in place for 5 min after each injection.

4-HT administration

For OPC ablation, 4-hydroxytamoxifen (4-HT; Sigma # H7904, St. Louis, MO) was injected into 2-3 months old *PDGFRα-CreER^{TM};ROSA26-iDTa* mice. A 20 mg/ml stock of 4-HT in 100% ethanol was prepared by sonication, and a 1 mg aliquot mixed 1:5 with sunflower oil. After evaporation of the ethanol by speedvac, 1 mg of 4-HT was injected intraperitoneally once daily for 5 consecutive days beginning 2 dpi.

CLARITY tissue clearing

Longitudinal slices of the dorsal spinal cord (<1mm thick) were optically cleared using the CLARITY protocol modified for passive clearing (Tomer et al., 2014). Adult mice that received unilateral L4 and L5 root crush, followed by AAV2-GFP intraganglionic injections, were perfused at 2 wpi with 20 ml of ice-cold 0.1 M PBS, followed by 20 ml of ice-cold hydrogel monomer solution [4% acrylamide (Bio-Rad, #161-0140), 0.25% azo-initiator (Wako, #VA-044), 4% Paraformaldehyde (Electron Microscopy Sciences, #15714-S) in PBS (Invitrogen, #70011-044)]. Each spinal cord was quickly dissected, its dorsal surface longitudinally sliced with attached dorsal roots, and the dorsal spinal cord placed in 20 ml of cold hydrogel in a 50 ml conical tube. After 24 hours at 4°C, the tube was placed in a desiccation chamber with its lid twisted open but not removed. The desiccation chamber was attached to a vacuum for 10 minutes, the chamber then purged with nitrogen gas, and the tube lid quickly screwed shut to prevent exposure to the outside air. The 50 ml tubes were placed in a 37°C water bath for 2 hours to allow for polymerization of the hydrogel and tissue. After polymerization, spinal cord was transferred into a 50 ml tube with clearing solution [20 mM lithium hydroxide monohydrate (Sigma-Aldrich, #254274), 200 mM boric acid (Sigma-Aldrich, #B7901), 4% SDS (Sigma-Aldrich, #L3771, pH to 8.5] and placed in an incubator with agitation at 37°C. Every 24 hours the clearing solution was replaced with fresh clearing solution for ~ 7 days or until the tissue had completely cleared. For microscopy, tissue was submerged in FocusClear (CelExplorer Labs Co., #FC-101) for 24 hours at 37°C to allow for refractive index matching. Tissue was then placed in an imaging well constructed on a standard microscope slide with a thin barrier of BluTack putty (Bostick, Fort Wayne, IN) sealed with a Willco-Dish **(**Ted Pella, #14032-120) and Kwik-Sil (World Precision Instruments, #KWIK-SIL).

Two-photon and widefield *in vivo* imaging

Both widefield and two-photon microscope set-ups were used for repeated imaging of DR axons at the DREZ in living mice, as we previously described (Skuba *et al.*, 2014). Widefield imaging was performed using a fluorescence stereomicroscope (M205C, Leica Microsystems) with a fast shutter and a CCD camera (ORCA-Rx2, Hamamatsu) controlled by MetaMorph software (Molecular Devices). Images were acquired either as single snapshots or as multiple streams of

10–20 frames acquired within 30–40 msec. exposure time. In-focus images were then selected, and an overview montage was created using Photoshop (Adobe Systems). A temperature controller (ATC 1000, World Precision Instruments, Inc.) and attached heating pad maintained the mouse's body temperature. For prolonged (>1 hr.) sessions, continuous inhalation anesthesia was consistently delivered via a laboratory animal anesthesia system (V-1 LAAS, VetEquip). 2-photon imaging was performed using an upright microscope optimized for confocal and multiphoton microscopy (TCS SP5 II, Leica Microsystems). After the mouse was mounted to a stereotaxic holder (SR-AM and STS-A, Narishige), imaging was performed with a Spectra Physics MaiTai laser tuned to ~890 nm for 2-photon excitation of YFP. Image acquisition used a 20X 0.7 NA water immersion lens controlled by Leica LAS AF software. For an axon ending of interest, a Z-stack was taken with line average every 1 µm throughout the entire focal area spanning 20-50 µm. Laser power and offset were adjusted to reduce background noise. If necessary, alignment software (Auto Aligner, Bitplane) was used to manually align off-centered optical sections. Maximum intensity projections along the Z-axis are presented as the final images.

Immunohistochemistry

Two or four weeks after DR crush, mice were sacrificed by an overdose of Euthasol and perfused transcardially with 0.9% saline followed by 4% paraformaldehyde (PFA) in 0.1 M PBS. The spinal cords with attached DRs and DRGs were removed and examined in wholemounts to exclude those tissues with poor transduction of AAV2-GFP and/or spared axons. Tissues were then processed for analysis on cryostat sections or as wholemounts. For analysis on cryostat sections, spinal cords were post-fixed in 4% PFA overnight at 4°C and cryoprotected in 30% sucrose for 24 hr. The tissues were then embedded in M-1 Embedding Matrix (Thermo Fisher Scientific, Waltham, MA), transversely sectioned at 20µm using a cryostat (Leica Microsystems, Germany), and mounted directly on slides (Superfrost Plus, Fisher Scientific, Pittsburgh, PA). For immunolabeling, sections were rinsed in PBS for 30 min. followed by 10 min. incubation with 0.1 M glycine in PBS, and 15 min. incubation with 0.2% Triton X-100, 2% bovine serum albumin (BSA) in PBS (TBP). Sections were incubated with primary antibodies overnight at 4°C, washed three times for 30 min. with 2% BSA in PBS, and incubated with secondary antibodies for 1 hr. at room temperature. After rinsing in PBS, sections were mounted in

Vectashield (Vector Laboratories, Burlingame, CA) and stored at –20°C until examination. For wholemount immunostaining of spinal cords, spinal cords with attached DRs were post-fixed in 4% PFA for 2 hr. at 4°C and the dura mater removed. The spinal cord was then rinsed with PBS for 30 min., incubated for 10 min. in 0.1 M glycine in 2% BSA/PBS, and permeabilized with pre-cooled methanol at –20°C for 10 min. After extensive rinsing in PBS, the spinal cord was incubated with primary antibody diluted in TBP at room temperature overnight, rinsed thoroughly in TBP the following day, and incubated with secondary antibodies for 2 hr. at room temperature. After rinsing in PBS, a thin slice of dorsal spinal cord (~2 mm thick) with attached DR stumps was cut with a microscissors and mounted on slides in Vectashield (Vector Laboratories).

Transmission and immunoelectron microscopy

For transmission electron microscopy, mice were perfused transcardially with 2% paraformaldehyde and 2.5% glutaraldehyde in 0.1 M Na-cacodylate buffer. Lumbar spinal cord segments (L3-L6) with attached DRs were removed as one piece, mounted on agarose support, and placed in the vibratome well. The most superficial longitudinal slice containing the DREZ (<250 μm thickness) was cut and further processed for TEM, as previously described (Di Maio *et al.*, 2011). For immunogold labeling of OPCs, mice were perfused with ice-cold 0.9% heparinized saline followed by 4% paraformaldehyde and 0.2% glutaraldehyde in 0.1M PBS (pH 7.4). After 2 hr. postfixation in the same fixative at 4°C, the spinal cord segment was embedded in 10% gelatin, cooled to 4°C, and a vibratome section of superficial spinal cord segment (~80 mm thickness) collected in PBS. The vibratome sections were then incubated with 1% sodium borohydride in PBS for 30 min., followed by permeabilization with 0.1% Triton-X-100 in PBS for 20 min. at 4°C. The sections were blocked with blocking solution (1% BSA, 3% NGS, 0.04% Triton-X-100 in PBS) for 30 min. and incubated with guinea pig anti-NG2 antibody (1:500, a gift from Dr. Dwight Bergles, Johns Hopkins University) diluted with blocking buffer for 24-48 hr. at 4°C. After rinsing, sections were incubated with 10 nm gold-conjugated goat anti-guinea pig IgG (1:200, Electron Microscopy Sciences, #25329) in blocking buffer for 3 hr. at room temperature. After rinsing, sections were post-fixed in 2% glutaraldehyde in PBS for 10 min. Silver enhancement was then performed in the dark with the HQ Silver Kit (Nanoprobes, NY) as directed by the manufacturer. Sections were post-fixed again with 1% osmium tetroxide in PBS

for 10 min. and then incubated with 2% uranyl acetate in ddH2O for 10 min. Sections were then dehydrated in an ascending ethanol series, followed by acetone series, and finally infiltrated with Araldite 502 Embed 812 resin. After polymerization, serial ultrathin sections (60–70 nm) were cut and mounted on Pioloform-coated slot grids. They were observed with a JEOL 1010 electron microscope at the Electron Microscopy Resource Lab, University of Pennsylvania.

Western blotting

The dura was removed from the spinal cord, which was then snap-frozen in liquid nitrogen and stored at -80ºC. Spinal cords were lysed in RIPA buffer (25 mM Tris pH 7.5, 150 mM NaCl, 1% Triton X-100, 0.5% sodium deoxycholate, 1 mM EDTA, 0.1% SDS). Lysis was for 40 min. on ice, followed by microcentrifugation at 14,000 rpm for 20 min. Protein concentration was determined using the BCA assay (ThermoFisher). Primary antibodies were used at the following concentrations for Western blots: rabbit anti-NG2 (Millipore, AB5320; 1:500), mouse anti-β-actin (Sigma, A5441; 1:1,000), and rat anti-PDGFRα (BD Biosciences, 558774; 1:500). Secondary antibodies for Western blots were HRP-conjugated goat anti-rabbit antibody (Santa Cruz, SC2030; 1:10,000), HRP-conjugated goat anti-mouse antibody (Jackson ImmunoResearch Laboratories, 115-035-174, 1:10,000), or HRP-conjugated goat anti-rat antibody (Jackson ImmunoResearch Laboratories, 112-035-003; 1:10,000). Blots were developed using ECL, ECL Plus (GE Healthcare, RPN2236).

Antibodies for immunohistochemistry

Primary antibodies were used at the following concentrations for immunohistochemistry: rabbit anti-glial fibrillary acidic protein (GFAP, N1506; 1:500), mouse anti-GFAP (Sigma, G3893; 1:500), goat anti-myelin oligodendrocyte glycoprotein (MOG; R&D Systems, AF2439; 1:200), mouse anti-SC2E (Cosmo Bio Co., CAC-GU01-M01AS-A; 1:10,000), goat anti-p75NGFR (Neuromics, GT15057; 1:500), rat anti-ED1 (AbD serotec, MCA1957; 1:400), rabbit anti-CGRP (Peninsula Lab., T-4032; 1:2,000), rabbit anti-NF200 (Sigma, N4142, 1:500), mouse anti-SV2 (Developmental Studies Hybridoma Bank, SV2; 1:10), guinea pig anti-NG2 (1:500, a gift from Dr. Dwight Bergles, Johns Hopkins University), rat anti-PDGFRα (BD Biosciences, 558774; 1:500), mouse anti adenomatous polyposis coli antigen (APC; clone CC1; Millipore, OP80-100UG; 1:100). Secondary antibodies were FITC conjugated goat anti-mouse IgG (Invitrogen,

A10530; 1:400), Alexa-Fluor 568-conjugated goat anti-mouse IgG (Invitrogen, A21124; 1:400), Alexa-Fluor 488-conjugated goat anti-rabbit IgG (Invitrogen, A11034; 1:400), Alexa-Flour 568 conjugated goat anti-rabbit IgG (Invitrogen, A11011; 1:400), Alexa-Flour 546 conjugated donkey anti-rabbit IgG (Invitrogen, A10040; 1:400), Alexa-Fluor 647-conjugated donkey anti-rabbit IgG (Invitrogen, A31573; 1:400), Alexa-Fluor 647-conjugated goat anti-rabbit IgG (Invitrogen, A21244; 1:400), Alexa-Flour 488 conjugated donkey anti-goat IgG (Invitrogen, A11055; 1:400), rhodamine (TRITC)-conjugated donkey anti-rat IgG (Jackson ImmunoResearch Laboratories, 712-025-150; 1:400), Cy3-conjugated donkey anti-guinea pig IgG (Jackson ImmunoResearch Laboratories, 706-166-148; 1:400), and Dye 647-conjugated donkey anti-guinea pig IgG (Jackson ImmunoResearch Laboratories, 706-606-148; 1:400).

OPC purification and co-culture with Percoll-purified DRG neurons

OPCs were isolated from P16-P18 C57BL/6 mice by immunopanning as previously described (Cahoy et al., 2008). Dissociated spinal cords were resuspended in panning buffer. To deplete microglia, the cell suspension was sequentially panned on two BSL1 panning plates (Vector Laboratories, #L1100). To purify OPCs, the cell suspension was then incubated on two PDGFRα plates coated with rat anti-PDGFRα IgG (BD Biosciences, 558774; 1:500). The adherent cells were washed with PBS to remove all antigen-negative nonadherent cells. The adherent cells were trypsinized and plated onto poly-D-lysine (PDL)-coated plates. The cultures were maintained under proliferating conditions by the addition of PDGFAA (Sigma, SRP3228; 10ng/ml) and bFGF (Sigma, SRP4038; 20 ng/ml) to the serum-free medium (DMEM, B27 supplement, 1X Sato supplement, 1X Trace Elements B, 10 ng/ml d-biotin, 2 mM Glutamine, 1 mM sodium pyruvate, 5 ug/ml insulin, 5 μg/ml N-acetyl-L-cysteine, 500 mM Forskolin, 100 U/ml Penicillin-streptomycin). Most cells (>95%) expressed OPC markers Olig2, NG2, and PDGFRα. After 5 days of incubation, percoll-purified DRG neurons were applied to cultured OPCs and cocultured for 5 days. For isolating DRG neurons, ~20 DRGs were removed from adult C57BL/6 mice and then dissociated in 1 ug/ml collagenase A and 2.4 U/ml dispase II. The dissociated DRGs were added to a two-layered Percoll gradient (12.5% Percoll layered over 28% Percoll solution with DMEM) and then subjected to density-gradient centrifugation. The interphase fraction was subsequently removed, spun, and resuspended in 20 μl of DMEM. A small amount of the cell

suspension (<5 μl**)** was added sparingly to cultured OPCs in the OPC proliferating medium. The cocultures were incubated in 5% CO_2 at 37ºC for 5 days.

Calcium imaging

Calcium imaging was performed using fura-2-based microfluorimetry and imaging analysis as we previously described (Dou et al., 2018). OPC-DRG neuron cocultures on coverslips were loaded with 4 μM of fura-2AM (Life Technologies, Grand Island, NY) for 30 min. at room temperature in HBSS, washed, and further incubated in normal bath solution (Tyrode's; 140 mM NaCl, 5 KCl mM, 2 CaCl2 mM, 1 MgCl2 mM, 10 HEPES mM, and 5.6 mM glucose). Coverslips were mounted in a small perfusion chamber (Warner Instruments, Model RC-25) and continuously perfused at 5–7 ml/min with Tyrode's solution. 100 nM capsaicin in Tyrode's solution, with or without 20μM CNQX and 10μM AP5, was locally infused for 20 sec., using a glass electrode (∼500 μm ID) positioned ~1.0 mm away from cells. Images were acquired at 3 s. intervals at room temperature using an Olympus inverted microscope equipped with a CCD camera (Hamamatsu, ORCA-03G). The fluorescence images were recorded and analyzed using the software MetaFluor 7.7.9 (Molecular Devices). The fluorescence ratio was determined as the fluorescence intensities excited at 340 and 380 nm with background subtraction.

Fluorescence microscopy, cell counting, and densitometric analysis

Z-stack fluorescent images were acquired on a Zeiss Axio Imager widefield microscope or on a Leica SP8 confocal microscope from 20μm serial transverse sections of spinal cords. Acquisition parameters were kept constant between different groups. Acquired images were merged using Imaris (Bitplane, Windsor, CT) and processed in Adobe Photoshop with minimal manipulations of brightness and contrast (Adobe Inc, San Jose, CA). For counting Ki67, Olig2, Iba1, ED1, and Sox10+ cells, 3 to 6 representative, non-adjacent sections taken from spinal cord segments of each mouse (n=3-6 per cohort) were carefully selected. Cell counting was performed blindly using ImageJ/Fiji (NIH). Immunoreactive cells were manually counted in ipsilateral regions of dorsal lateral funiculus, dorsal root, or dorsal spinal cord, and then averaged by the number of evaluated sections and animals. For comparative analysis of OPC ablation, CSPG deletion, GFAP, and p75 immunoreactivity, images were converted to grayscale, subthresholded to the background, and calculated using ImageJ/Fiji (NIH). Intensity was defined as the average gray

value obtained from all pixels within the region of interest above background. Data are presented as the mean fluorescence intensities (MFI) in each region of interest, calculated by subtracting the mean value of randomly selected background regions lacking immunoreactivity of interest.

Analysis of axon regeneration across the DREZ

The DREZ was defined as the ~100μm wide CNS territory beyond the boundary between the CNS and PNS. The yellow dotted lines (e.g., Figure 3A) denote the boundary (termed also borderline or border), demarcated by GFAP immunolabeling of astrocytic processes that extend peripherally. When GFAP was not immunolabeled, the borderline was identified based on the greater abundance of cell nuclei in the PNS than CNS (Zhai *et al.*, 2021). For comparative evaluation of regeneration, we considered that an axon penetrated the DREZ when it extended at least 100μm beyond the borderline. For quantitative analysis, digital images were captured from 3 to 6 representative, non-adjacent sections taken from spinal cord segments of each mouse (n = 3–6 mice per cohort). A raw image was converted to a binary image using ImageJ with a threshold that appropriately separated GFP and background fluorescence. Lines were drawn at 100μm before the borderline in the PNS, at the borderline, and at 100μm intervals into CNS territory. The number of intersections of GFP+ axons at these distances was counted. The number of axons that crossed the border was normalized by the number of GFP+ axons counted at 100μm before the borderline in the PNS, and then averaged by the number of evaluated sections and animals. This quantification resulted in the 'axon number index' that indicated the relative number and distance of axons that regenerated into the CNS or spinal cord.

Statistical analysis

All statistical analyses were performed using PRISM 9.0 (GraphPad). Statistical analysis was done using the two-sample Mann-Whitney test or unpaired t-test for two-group comparisons, and analysis of variance (ANOVA) with Tukey's or Sidak's test for multiple comparisons, as appropriate. All data were presented as mean ± SEM or SD as indicated in the figure legend. A p-value of 0.05 or less was considered statistically significant.

SUPPLEMENTAL INFORMATION

Supplemental figures and figure legends – 8 figures

Supplemental experimental procedures - TBD

REFERENCES

Afshari, F.T., Kwok, J.C., and Fawcett, J.W. (2010). Astrocyte-produced ephrins inhibit schwann cell migration via VAV2 signaling. J Neurosci *30*, 4246-4255. 30/12/4246 [pii]10.1523/JNEUROSCI.3351-09.2010.

Akay, L.A., Effenberger, A.H., and Tsai, L.H. (2021). Cell of all trades: oligodendrocyte precursor cells in synaptic, vascular, and immune function. Genes Dev *35*, 180-198. 10.1101/gad.344218.120.

Andreae, L.C., and Burrone, J. (2014). The role of neuronal activity and transmitter release on synapse formation. Curr Opin Neurobiol *27*, 47-52. 10.1016/j.conb.2014.02.008.

Bergles, D.E., and Richardson, W.D. (2015). Oligodendrocyte Development and Plasticity. Cold Spring Harb Perspect Biol *8*, a020453. 10.1101/cshperspect.a020453.

Bergles, D.E., Roberts, J.D., Somogyi, P., and Jahr, C.E. (2000). Glutamatergic synapses on oligodendrocyte precursor cells in the hippocampus. Nature *405*, 187-191. 10.1038/35012083.

Birey, F., and Aguirre, A. (2015). Age-Dependent Netrin-1 Signaling Regulates NG2+ Glial Cell Spatial Homeostasis in Normal Adult Gray Matter. J Neurosci *35*, 6946-6951. 10.1523/jneurosci.0356-15.2015.

Birey, F., Kloc, M., Chavali, M., Hussein, I., Wilson, M., Christoffel, D.J., Chen, T., Frohman, M.A., Robinson, J.K., Russo, S.J., et al. (2019). Genetic and Stress-Induced Loss of NG2 Glia Triggers Emergence of Depressive-like Behaviors through Reduced Secretion of FGF2. Neuron *104*, 825-826. 10.1016/j.neuron.2019.11.005.

Blanquie, O., and Bradke, F. (2018). Cytoskeleton dynamics in axon regeneration. Curr Opin Neurobiol *51*, 60-69. 10.1016/j.conb.2018.02.024.

Brockschnieder, D., Lappe-Siefke, C., Goebbels, S., Boesl, M.R., Nave, K.A., and Riethmacher, D. (2004). Cell depletion due to diphtheria toxin fragment A after Cre-mediated recombination. Mol Cell Biol *24*, 7636-7642. 10.1128/mcb.24.17.7636-7642.2004.

Busch, S.A., Horn, K.P., Silver, D.J., and Silver, J. (2009). Overcoming macrophage-mediated axonal dieback following CNS injury. J Neurosci *29*, 9967-9976. 29/32/9967 [pii] 10.1523/JNEUROSCI.1151-09.2009.

Cahoy, J.D., Emery, B., Kaushal, A., Foo, L.C., Zamanian, J.L., Christopherson, K.S., Xing, Y., Lubischer, J.L., Krieg, P.A., Krupenko, S.A., et al. (2008). A transcriptome database for astrocytes, neurons, and oligodendrocytes: a new resource for understanding brain development and function. J Neurosci *28*, 264-278. 10.1523/jneurosci.4178-07.2008.

Carlstedt, T. (1985). Regenerating axons form nerve terminals at astrocytes. Brain Res *347*, 188-191. 0006-8993(85)90911-4 [pii].

Carlstedt, T., Dalsgaard, C.J., and Molander, C. (1987). Regrowth of lesioned dorsal root nerve fibers into the spinal cord of neonatal rats. Neurosci Lett *74*, 14-18.

Chong, M.S., Woolf, C.J., Haque, N.S., and Anderson, P.N. (1999). Axonal regeneration from injured dorsal roots into the spinal cord of adult rats. J Comp Neurol *410*, 42-54. 10.1002/(SICI)1096-9861(19990719)410:1<42::AID-CNE5>3.0.CO;2-F [pii].

Cregg, J.M., DePaul, M.A., Filous, A.R., Lang, B.T., Tran, A., and Silver, J. (2014). Functional regeneration beyond the glial scar. Exp Neurol *253*, 197-207. 10.1016/j.expneurol.2013.12.024.

Di Maio, A., Skuba, A., Himes, B.T., Bhagat, S.L., Hyun, J.K., Tessler, A., Bishop, D., and Son, Y.J. (2011). In Vivo Imaging of Dorsal Root Regeneration: Rapid Immobilization and Presynaptic Differentiation at the CNS/PNS Border. J Neurosci *31*, 4569-4582. 31/12/4569 [pii] 10.1523/JNEUROSCI.4638-10.2011.

Djogo, T., Robins, S.C., Schneider, S., Kryzskaya, D., Liu, X., Mingay, A., Gillon, C.J., Kim, J.H., Storch, K.F., Boehm, U., et al. (2016). Adult NG2-Glia Are Required for Median Eminence-Mediated Leptin Sensing and Body Weight Control. Cell Metab *23*, 797-810. 10.1016/j.cmet.2016.04.013.

Dorrier, C.E., Aran, D., Haenelt, E.A., Sheehy, R.N., Hoi, K.K., Pintarić, L., Chen, Y., Lizama, C.O., Cautivo, K.M., Weiner, G.A., et al. (2021). CNS fibroblasts form a fibrotic scar in response to immune cell infiltration. Nat Neurosci *24*, 234-244. 10.1038/s41593-020-00770-9.

Dou, Y., Xia, J., Gao, R., Gao, X., Munoz, F.M., Wei, D., Tian, Y., Barrett, J.E., Ajit, S., Meucci, O., et al. (2018). Orai1 Plays a Crucial Role in Central Sensitization by Modulating Neuronal Excitability. J Neurosci *38*, 887-900. 10.1523/jneurosci.3007-17.2017.

Evans, T.A., Barkauskas, D.S., Myers, J.T., Hare, E.G., You, J.Q., Ransohoff, R.M., Huang, A.Y., and Silver, J. (2014). High-resolution intravital imaging reveals that blood-derived macrophages but not resident microglia facilitate secondary axonal dieback in traumatic spinal cord injury. Exp Neurol *254*, 109-120. 10.1016/j.expneurol.2014.01.013.

Feng, G.P., Mellor, R.H., Bernstein, M., Keller-Peck, C., Nguyen, Q.T., Wallace, M., Nerbonne, J.M., Lichtman, J.W., and Sanes, J.R. (2000). Imaging neuronal subsets in transgenic mice expressing multiple spectral variants of GFP. Neuron *28*, 41-51. 10.1016/s0896-6273(00)00084-2.

Filous, A.R., Tran, A., Howell, C.J., Busch, S.A., Evans, T.A., Stallcup, W.B., Kang, S.H., Bergles, D.E., Lee, S.I., Levine, J.M., and Silver, J. (2014). Entrapment via synaptic-like connections between NG2 proteoglycan+ cells and dystrophic axons in the lesion plays a role in regeneration failure after spinal cord injury. J Neurosci *34*, 16369-16384. 10.1523/jneurosci.1309-14.2014.

Fraher, J. (2002). Axons and glial interfaces: ultrastructural studies. J Anat *200*, 415-430. 10.1046/j.1469-7580.2002.00037.x.

Friedman, H.V., Bresler, T., Garner, C.C., and Ziv, N.E. (2000). Assembly of new individual excitatory synapses: time course and temporal order of synaptic molecule recruitment. Neuron *27*, 57-69. 10.1016/s0896-6273(00)00009-x.

Gerber, D., Pereira, J.A., Gerber, J., Tan, G., Dimitrieva, S., Yángüez, E., and Suter, U. (2021). Transcriptional profiling of mouse peripheral nerves to the single-cell level to build a sciatic nerve ATlas (SNAT). eLife *10*. 10.7554/eLife.58591.

Golding, J.P., Shewan, D., Berry, M., and Cohen, J. (1996). An in vitro model of the rat dorsal root entry zone reveals developmental changes in the extent of sensory axon growth into the spinal cord. Mol Cell Neurosci *7*, 191-203. 10.1006/mcne.1996.0015.

He, Z., and Jin, Y. (2016). Intrinsic Control of Axon Regeneration. Neuron *90*, 437-451. 10.1016/j.neuron.2016.04.022.

Held, R.G., Liu, C., Ma, K., Ramsey, A.M., Tarr, T.B., De Nola, G., Wang, S.S.H., Wang, J., van den Maagdenberg, A., Schneider, T., et al. (2020). Synapse and Active Zone Assembly in the Absence of Presynaptic Ca(2+) Channels and Ca(2+) Entry. Neuron *107*, 667-683.e669. 10.1016/j.neuron.2020.05.032.

Hill, C.E. (2017). A view from the ending: Axonal dieback and regeneration following SCI. Neurosci Lett *652*, 11-24. 10.1016/j.neulet.2016.11.002.

Hilton, B.J., Husch, A., Schaffran, B., Lin, T.C., Burnside, E.R., Dupraz, S., Schelski, M., Kim, J., Müller, J.A., Schoch, S., et al. (2022). An active vesicle priming machinery suppresses axon regeneration upon adult CNS injury. Neuron *110*, 51-69.e57. 10.1016/j.neuron.2021.10.007.

Hughes, A.N., and Appel, B. (2019). Oligodendrocytes express synaptic proteins that modulate myelin sheath formation. Nature communications *10*, 4125. 10.1038/s41467-019-12059-y.

Hughes, E.G., Kang, S.H., Fukaya, M., and Bergles, D.E. (2013). Oligodendrocyte progenitors balance growth with self-repulsion to achieve homeostasis in the adult brain. Nat Neurosci *16*, 668-676. 10.1038/nn.3390.

Kaiser, R., Waldauf, P., Ullas, G., and Krajcová, A. (2020). Epidemiology, etiology, and types of severe adult brachial plexus injuries requiring surgical repair: systematic review and meta-analysis. Neurosurgical review *43*, 443-452. 10.1007/s10143-018-1009-2.

Kula, B., Chen, T.J., and Kukley, M. (2019). Glutamatergic signaling between neurons and oligodendrocyte lineage cells: Is it synaptic or non-synaptic? Glia *67*, 2071-2091. 10.1002/glia.23617.

Labbé, K., and Saleh, M. (2008). Cell death in the host response to infection. Cell Death Differ *15*, 1339-1349. 10.1038/cdd.2008.91.

Laredo, F., Plebanski, J., and Tedeschi, A. (2019). Pericytes: Problems and Promises for CNS Repair. Frontiers in cellular neuroscience *13*, 546. 10.3389/fncel.2019.00546.

Li, M., Shibata, A., Li, C., Braun, P.E., McKerracher, L., Roder, J., Kater, S.B., and David, S. (1996). Myelin-associated glycoprotein inhibits neurite/axon growth and causes growth cone collapse. J Neurosci Res *46*, 404-414. 10.1002/(SICI)1097-4547(19961115)46:4<404::AID-JNR2>3.0.CO;2-K [pii] 10.1002/(SICI)1097-4547(19961115)46:4<404::AID-JNR2>3.0.CO;2-K.

Li, Y., Carlstedt, T., Berthold, C.H., and Raisman, G. (2004). Interaction of transplanted olfactory-ensheathing cells and host astrocytic processes provides a bridge for axons to regenerate across the dorsal root entry zone. Exp Neurol *188*, 300-308. 10.1016/j.expneurol.2004.04.021.

Liu, Y., and Aguzzi, A. (2020). NG2 glia are required for maintaining microglia homeostatic state. Glia *68*, 345-355. 10.1002/glia.23721.

Liu, Y., Keefe, K., Tang, X., Lin, S., and Smith, G.M. (2014). Use of self-complementary adeno-associated virus serotype 2 as a tracer for labeling axons: implications for axon regeneration. PLoS One *9*, e87447. 10.1371/journal.pone.0087447.

Liuzzi, F.J., and Lasek, R.J. (1987). Astrocytes block axonal regeneration in mammals by activating the physiological stop pathway. Science *237*, 642-645.

Lorenzana, A.O., Lee, J.K., Mui, M., Chang, A., and Zheng, B. (2015). A surviving intact branch stabilizes remaining axon architecture after injury as revealed by in vivo imaging in the mouse spinal cord. Neuron *86*, 947-954. 10.1016/j.neuron.2015.03.061.

Lucido, A.L., Suarez Sanchez, F., Thostrup, P., Kwiatkowski, A.V., Leal-Ortiz, S., Gopalakrishnan, G., Liazoghli, D., Belkaid, W., Lennox, R.B., Grutter, P., et al. (2009). Rapid assembly of functional presynaptic boutons triggered by adhesive contacts. J Neurosci *29*, 12449-12466. 10.1523/jneurosci.1381-09.2009.

Mar, F.M., Simões, A.R., Rodrigo, I.S., and Sousa, M.M. (2016). Inhibitory Injury Signaling Represses Axon Regeneration After Dorsal Root Injury. Mol Neurobiol *53*, 4596-4605. 10.1007/s12035-015-9397-6.

Mount, C.W., Yalçın, B., Cunliffe-Koehler, K., Sundaresh, S., and Monje, M. (2019). Monosynaptic tracing maps brain-wide afferent oligodendrocyte precursor cell connectivity. eLife *8*. 10.7554/eLife.49291.

Osterstock, G., Le Bras, B., Arulkandarajah, K.H., Le Corronc, H., Czarnecki, A., Mouffle, C., Bullier, E., Legendre, P., and Mangin, J.M. (2018). Axoglial synapses are formed onto pioneer oligodendrocyte precursor cells at the onset of spinal cord gliogenesis. Glia *66*, 1678-1694. 10.1002/glia.23331.

Partyka, P.P., Jin, Y., Bouyer, J., DaSilva, A., Godsey, G.A., Nagele, R.G., Fischer, I., and Galie, P.A. (2019). Harnessing neurovascular interaction to guide axon growth. Scientific reports *9*, 2190. 10.1038/s41598-019-38558-y.

Passlick, S., Trotter, J., Seifert, G., Steinhäuser, C., and Jabs, R. (2016). The NG2 Protein Is Not Required for Glutamatergic Neuron-NG2 Cell Synaptic Signaling. Cereb Cortex *26*, 51-57. 10.1093/cercor/bhu171.

Pinto, M.J., and Almeida, R.D. (2016). Puzzling out presynaptic differentiation. J Neurochem *139*, 921-942. 10.1111/jnc.13702.

Skaper, S.D. (2019). Oligodendrocyte precursor cells as a therapeutic target for demyelinating diseases. Prog Brain Res *245*, 119-144. 10.1016/bs.pbr.2019.03.013.

Skuba, A., Manire, M.A., Kim, H., Han, S.B., and Son, Y.J. (2014). Time-lapse in vivo imaging of dorsal root nerve regeneration in mice. Methods Mol Biol *1162*, 219-232. 10.1007/978-1-4939-0777-9_18.

Smith, G.M., Falone, A.E., and Frank, E. (2012). Sensory axon regeneration: rebuilding functional connections in the spinal cord. Trends Neurosci *35*, 156-163. 10.1016/j.tins.2011.10.006.

Soderblom, C., Luo, X., Blumenthal, E., Bray, E., Lyapichev, K., Ramos, J., Krishnan, V., Lai-Hsu, C., Park, K.K., Tsoulfas, P., and Lee, J.K. (2013). Perivascular fibroblasts form the fibrotic scar after contusive spinal cord injury. J Neurosci *33*, 13882-13887. 10.1523/jneurosci.2524-13.2013.

Son, Y.J. (2015). Synapsing with NG2 cells (polydendrocytes), unappreciated barrier to axon regeneration? Neural regeneration research *10*, 346-348. 10.4103/1673-5374.153672.

Südhof, T.C. (2018). Towards an Understanding of Synapse Formation. Neuron *100*, 276-293. 10.1016/j.neuron.2018.09.040.

Szallasi, A., and Blumberg, P.M. (1999). Vanilloid (Capsaicin) receptors and mechanisms. Pharmacol Rev *51*, 159-212.

Tamburini, E., Dallatomasina, A., Quartararo, J., Cortelazzi, B., Mangieri, D., Lazzaretti, M., and Perris, R. (2019). Structural deciphering of the NG2/CSPG4 proteoglycan multifunctionality. Faseb j *33*, 3112-3128. 10.1096/fj.201801670R.

Tedeschi, A., Dupraz, S., Laskowski, C.J., Xue, J., Ulas, T., Beyer, M., Schultze, J.L., and Bradke, F. (2016). The Calcium Channel Subunit Alpha2delta2 Suppresses Axon Regeneration in the Adult CNS. Neuron *92*, 419-434. 10.1016/j.neuron.2016.09.026.

Tom, V.J., Steinmetz, M.P., Miller, J.H., Doller, C.M., and Silver, J. (2004). Studies on the development and behavior of the dystrophic growth cone, the hallmark of regeneration failure, in an in vitro model of the glial scar and after spinal cord injury. J Neurosci *24*, 6531-6539. 10.1523/JNEUROSCI.0994-04.2004 24/29/6531 [pii].

Tomer, R., Ye, L., Hsueh, B., and Deisseroth, K. (2014). Advanced CLARITY for rapid and high-resolution imaging of intact tissues. Nat Protoc *9*, 1682-1697. 10.1038/nprot.2014.123.

Tomita, Y., Horiuchi, K., Kano, K., Tatsukawa, T., Matsuo, R., Hayasaka, T., Yoshida, Y., Kabara, M., Yasuda, S., Nakajima, K., et al. (2019). Ninjurin 1 mediates peripheral nerve regeneration through Schwann cell maturation of NG2-positive cells. Biochem Biophys Res Commun *519*, 462-468. 10.1016/j.bbrc.2019.09.007.

Tran, A.P., Warren, P.M., and Silver, J. (2018). The Biology of Regeneration Failure and Success After Spinal Cord Injury. Physiol Rev *98*, 881-917. 10.1152/physrev.00017.2017.

Varadarajan, S.G., Hunyara, J.L., Hamilton, N.R., Kolodkin, A.L., and Huberman, A.D. (2022). Central nervous system regeneration. Cell *185*, 77-94. 10.1016/j.cell.2021.10.029.

Vargas, M.E., and Barres, B.A. (2007). Why is Wallerian degeneration in the CNS so slow? Annu Rev Neurosci *30*, 153-179. 10.1146/annurev.neuro.30.051606.094354.

Verhage, M., Maia, A.S., Plomp, J.J., Brussaard, A.B., Heeroma, J.H., Vermeer, H., Toonen, R.F., Hammer, R.E., van den Berg, T.K., Missler, M., et al. (2000). Synaptic assembly of the brain in the absence of neurotransmitter secretion. Science *287*, 864-869. 10.1126/science.287.5454.864.

Warren, P.M., Andrews, M.R., Smith, M., Bartus, K., Bradbury, E.J., Verhaagen, J., Fawcett, J.W., and Kwok, J.C.F. (2020). Secretion of a mammalian chondroitinase ABC aids glial integration at PNS/CNS boundaries. Scientific reports *10*, 11262. 10.1038/s41598-020-67526-0.

Weinrauch, Y., and Zychlinsky, A. (1999). The induction of apoptosis by bacterial pathogens. Annual review of microbiology *53*, 155-187. 10.1146/annurev.micro.53.1.155.

Wiliams, R.R., and Bunge, M.B. (2012). Schwann cell transplantation: a repair strategy for spinal cord injury? Prog Brain Res *201*, 295-312. 10.1016/b978-0-444-59544-7.00014-7.

Wu, D., Jin, Y., Shapiro, T.M., Hinduja, A., Baas, P.W., and Tom, V.J. (2020). Chronic neuronal activation increases dynamic microtubules to enhance functional axon regeneration after dorsal root crush injury. Nature communications *11*, 6131. 10.1038/s41467-020-19914-3.

Xiao, Y., Petrucco, L., Hoodless, L.J., Portugues, R., and Czopka, T. (2022). Oligodendrocyte precursor cells sculpt the visual system by regulating axonal remodeling. Nat Neurosci *25*, 280-284. 10.1038/s41593-022-01023-7.

Zhai, J., Kim, H., Han, S.B., Manire, M., Yoo, R., Pang, S., Smith, G.M., and Son, Y.J. (2021). Co-targeting myelin inhibitors and CSPGs markedly enhances regeneration of GDNF-stimulated, but not conditioning-lesioned, sensory axons into the spinal cord. eLife *10*. 10.7554/eLife.63050.

Zukor, K., Belin, S., Wang, C., Keelan, N., Wang, X., and He, Z. (2013). Short hairpin RNA against PTEN enhances regenerative growth of corticospinal tract axons after spinal cord injury. J Neurosci *33*, 15350-15361. 10.1523/jneurosci.2510-13.2013.

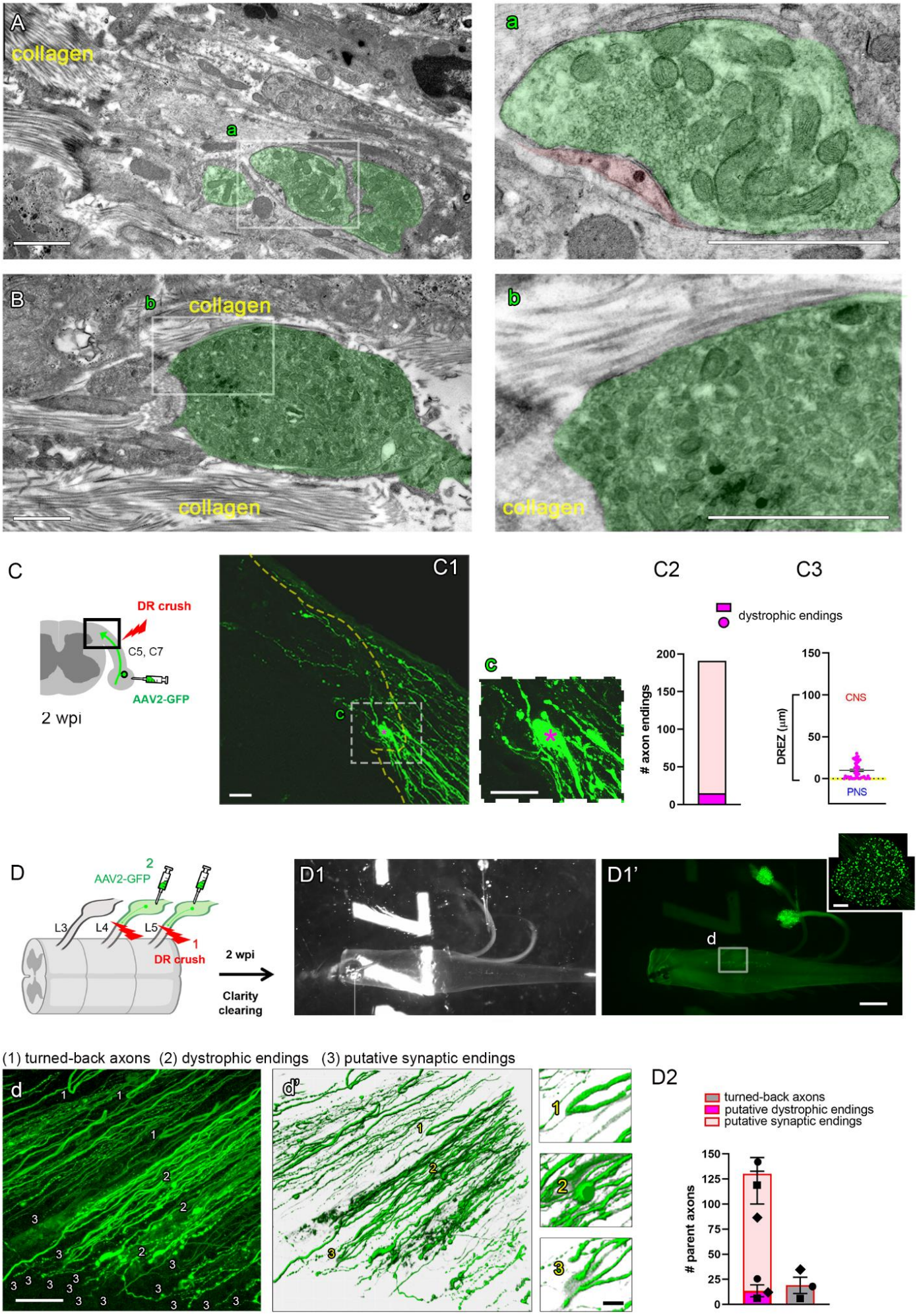
A
collagen
a
a
B
b
collagen
collagen
b
collagen
C
DR crush
C5, C7
AAV2-GFP
2 wpi
C1
c
c
C2
C3
dystrophic endings
axon endings
200
150
100
50
0
150
100
50
0
DREZ (µm)
CNS
PNS
D
2
AAV2-GFP
L3
L4
L5
1
DR crush
2 wpi
Clarity clearing
D1
D1'
d
(1) turned-back axons (2) dystrophic endings (3) putative synaptic endings
d
d'
1
2
3
D2
turned-back axons
putative dystrophic endings
putative synaptic endings
parent axons
150
125
100
75
50
25
0

Figure 1. Dystrophic endings form by axons embedded in collagens at the borderline

(A, B) Ultrastructural comparison of a synaptic ending (A) and a dystrophic ending (B), with corresponding enlarged views (a, b), formed by DR axons (Green) at the DREZ at 2 wpi. The presynaptic ending is small, organized, and apposed to an unknown postsynaptic cell (Red; a), whereas the dystrophic ending is large, disorganized, and embedded in acellular collagen fibers (B, b). Scale bar: 500nm

(C-C3) The incidence and location of dystrophic endings analyzed on transverse sections, at 2 weeks after C5-C8 root crush followed by AAV2-GFP injections to C5 and C7 DRGs (C). A representative section (C1), with enlarged view (c), showing a large dystrophic ending (asterisk) formed at the borderline (dotted line). Note that many other axons stopped past the borderline do not display dystrophic endings. Representative quantification of a mouse showing the incidence of dystrophic endings (C2) and their location relative to the borderline (C3) (n=191 axons, >15 serial sections). Scale bar: 20μm

(D-D2) High resolution 3D imaging and quantitative analysis of different axon endings on wholemounts of CLARITY cleared spinal cords at 2 weeks after L4 and L5 root crush (D). Transmitted light (D1) and fluorescent (D1', d, d') views of a representative cleared spinal cord, roots, DRG (inset in D1'), and GFP+ axons arrested at the DREZ in enlarged (d) or volume rendered images (d'). Representative examples illustrate parental axons that turn around (e.g., d'-1), form a large dystrophic ending (e.g., d'-2), or form a small putative synaptic ending (e.g., d'-3). Relative incidence of different axon endings illustrating that a limited number of parental axons turned around or stopped by forming dystrophic endings (D2). n= >100 axons/mouse, 3 mice. Scale bars: 200μm (D1, D1'), 50μm (D1', inset), 50μm (d, d'), 10μm (d'1-3)

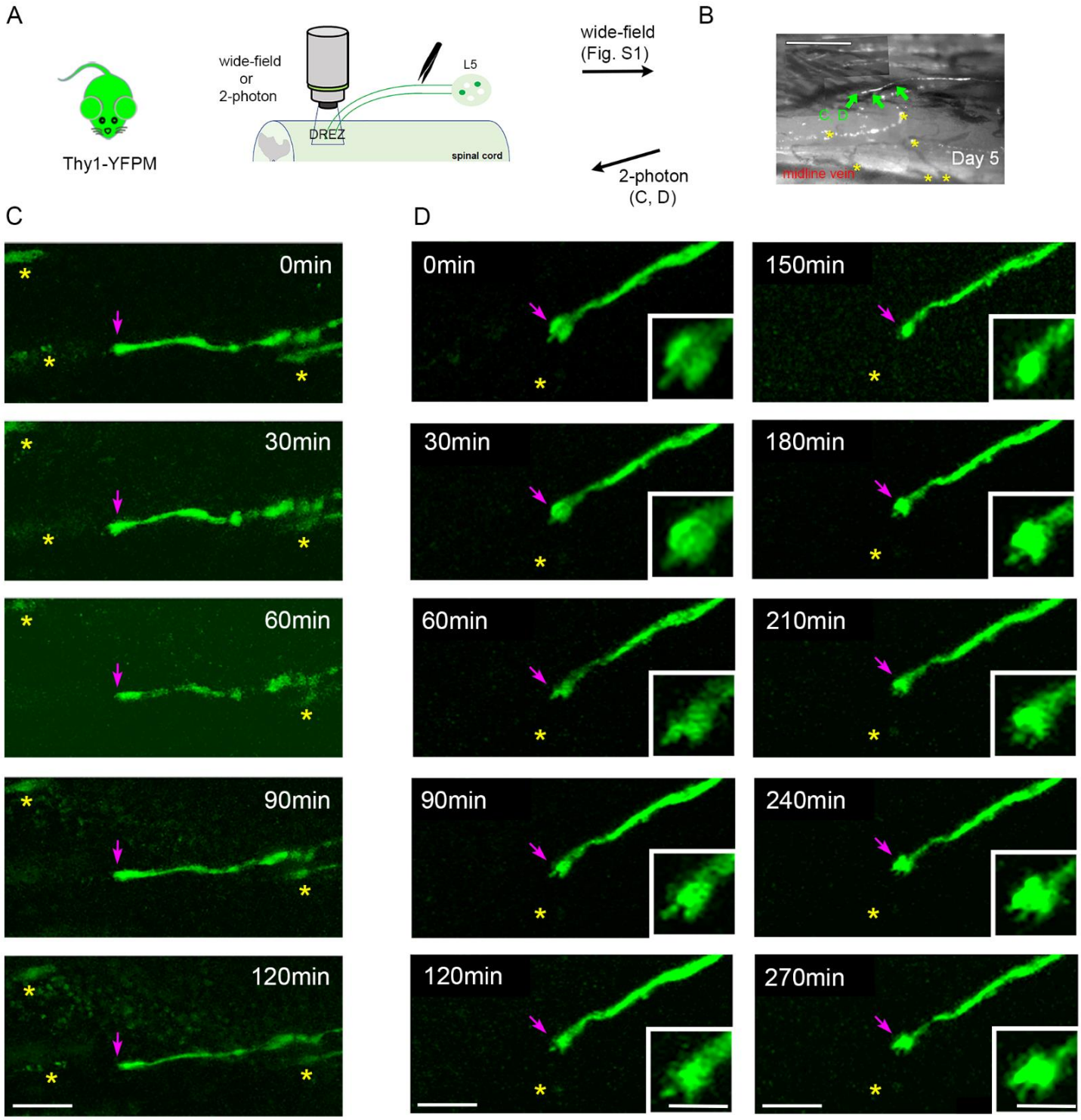

Figure 2. Two-photon imaging confirms rapid axon immobilization at the DREZ

(A) Schematic illustration of the experimental procedure for two-photon imaging of DR axons in live Thy1-YFPM mice after L5 root crush.

(B) A widefield view of the DREZ area, taken at 5 dpi, showing an axon of interest (arrows) and fluorescent debris of degenerating old axons and a midline vein that served as landmarks (asterisks). Subsequent imaging sessions of this axon are shown in **Figure S1**. Scale bar:100µm

(C, D) Two-photon imaging of representative axon tips with either slender (C) or small roundish shape (D), taken every 30 min on 5 dpi. Arrows denote immobile axon tips and asterisks denote landmarks. Scale bar: 50µm (C, D), 20µm (D, insets)

Related data are available in **Figure S1**.

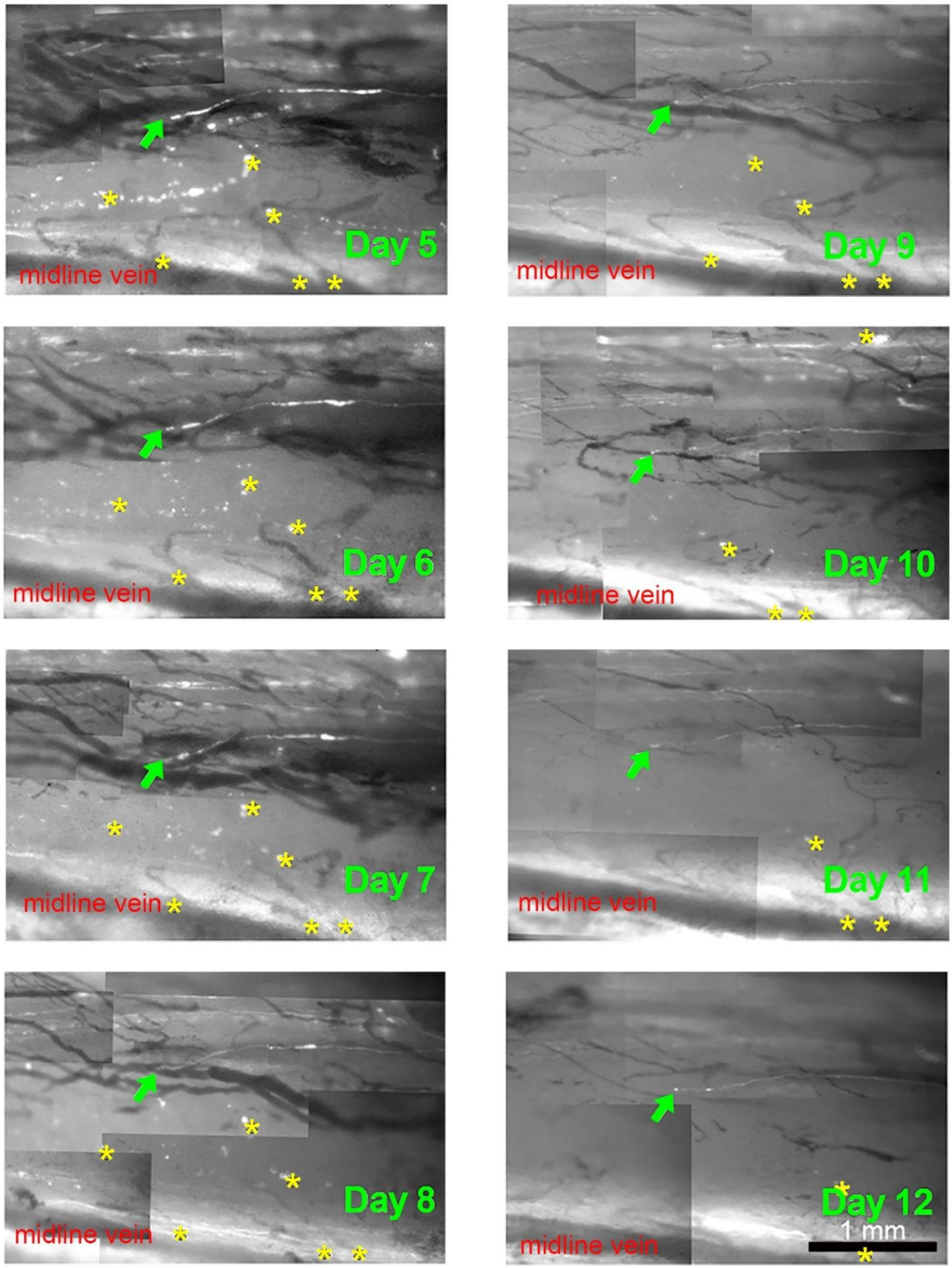

Figure S1. Daily *in vivo* monitoring of the same axons following two-photon imaging
Widefield *in vivo* images of the same axon taken daily after two-photon imaging on 4 or 5 dpi, illustrating that the axon tip (arrows) does not degenerate, excluding that immobility is due to phototoxicity. Asterisks denote axon debris and branching points of blood vessels that served as landmarks. Scale bar: 1mm

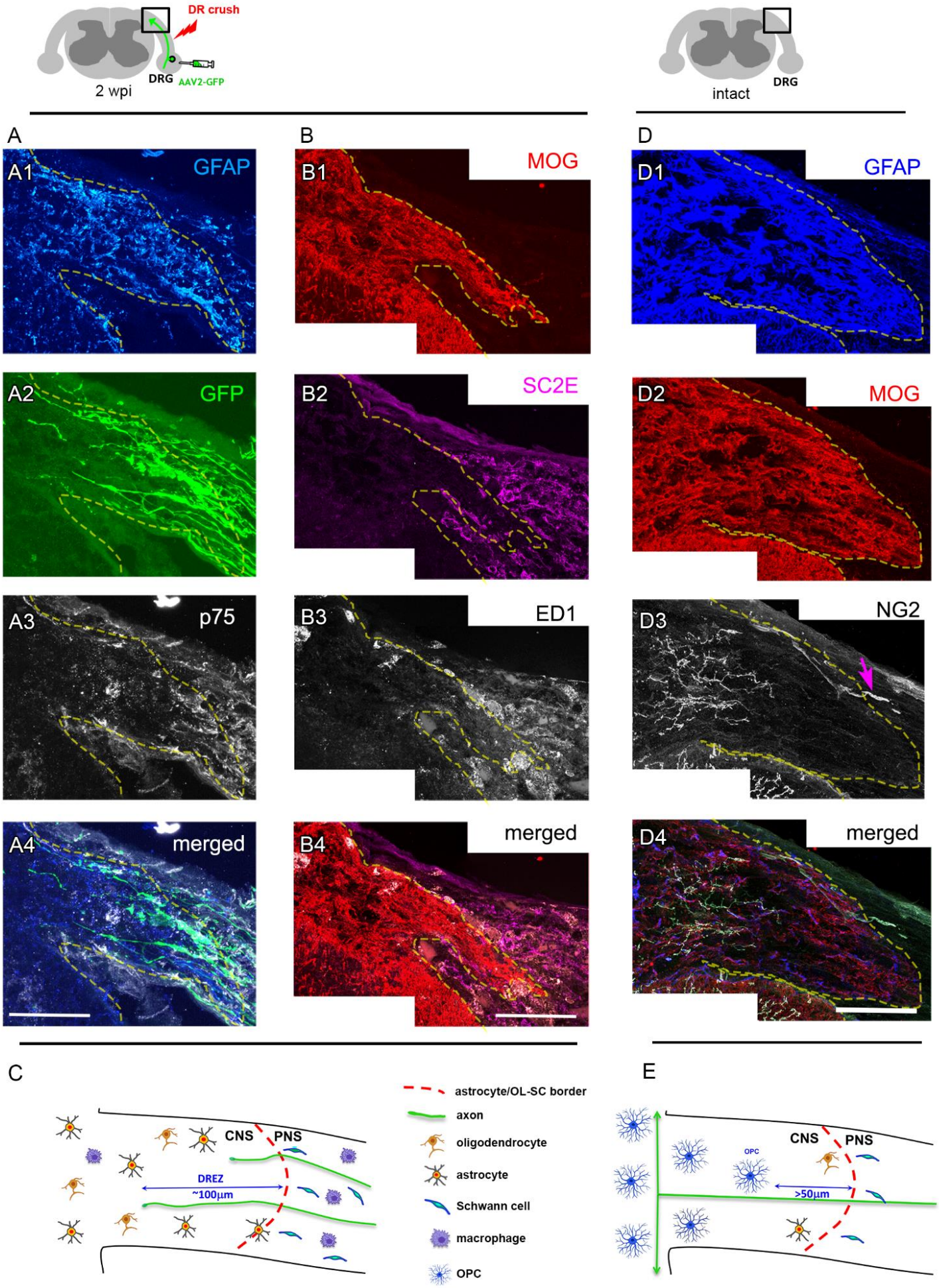
DR crush
DRG
AAV2-GFP
2 wpi
intact
DRG
A
B
D
A1
GFAP
B1
MOG
D1
GFAP
A2
GFP
B2
SC2E
D2
MOG
A3
p75
B3
ED1
D3
NG2
A4
merged
B4
merged
D4
merged
C
CNS
PNS
DREZ
~100µm
astrocyte/OL-SC border
axon
oligodendrocyte
astrocyte
Schwann cell
macrophage
OPC
E
CNS
PNS
OPC
>50µm

Figure 3. OPCs are absent at the borderline; the location of other glia is unrelated to axon arrest

(A, B) Transverse sections of a spinal cord 2 weeks after cervical root crush followed by intraganglionic injection of AAV2-GFP.

(A) A DREZ area illustrating spatial relationships of arrested GFP+ axons (A2) with GFAP-labeled astrocytes (A1) and p75-labeled Schwann cell processes (A3). Many axons extend across the borderline (dotted line) by growing through astrocytic processes without association with leading Schwann cell processes. Scale bar: 50μm

(B) A DREZ area illustrating spatial relationships of arrested axons (refer to A2) with MOG-labeled oligodendrocytes (B1), SC2E-labeled myelinating Schwann cells (B2), and ED1-labeled macrophages (B3). Macrophages are enriched peripherally but sparse at the DREZ. Scale bar: 50μm

(C) Diagram summarizing insignificant spatial relationships of arrested axons with oligodendrocytes, astrocytes, Schwann cells, and macrophages at axotomized DREZ.

(D) A DREZ area of uninjured DRs illustrating that NG2-labeled OPCs (D3) are absent at and immediately near the borderline (dotted line), denoted by astrocytes (D1) and oligodendrocytes (D2), but abundant deeper in CNS territory (>50μm from the borderline). Arrow in D3 denotes NG2-labeled pericytes associated with a blood vessel. Scale bar: 50μm

(E) Diagram illustrating the distance and position of OPC processes relative to the borderline (dotted line) at intact DREZ with no axon injury.

Related data are available in **Figure S2**.

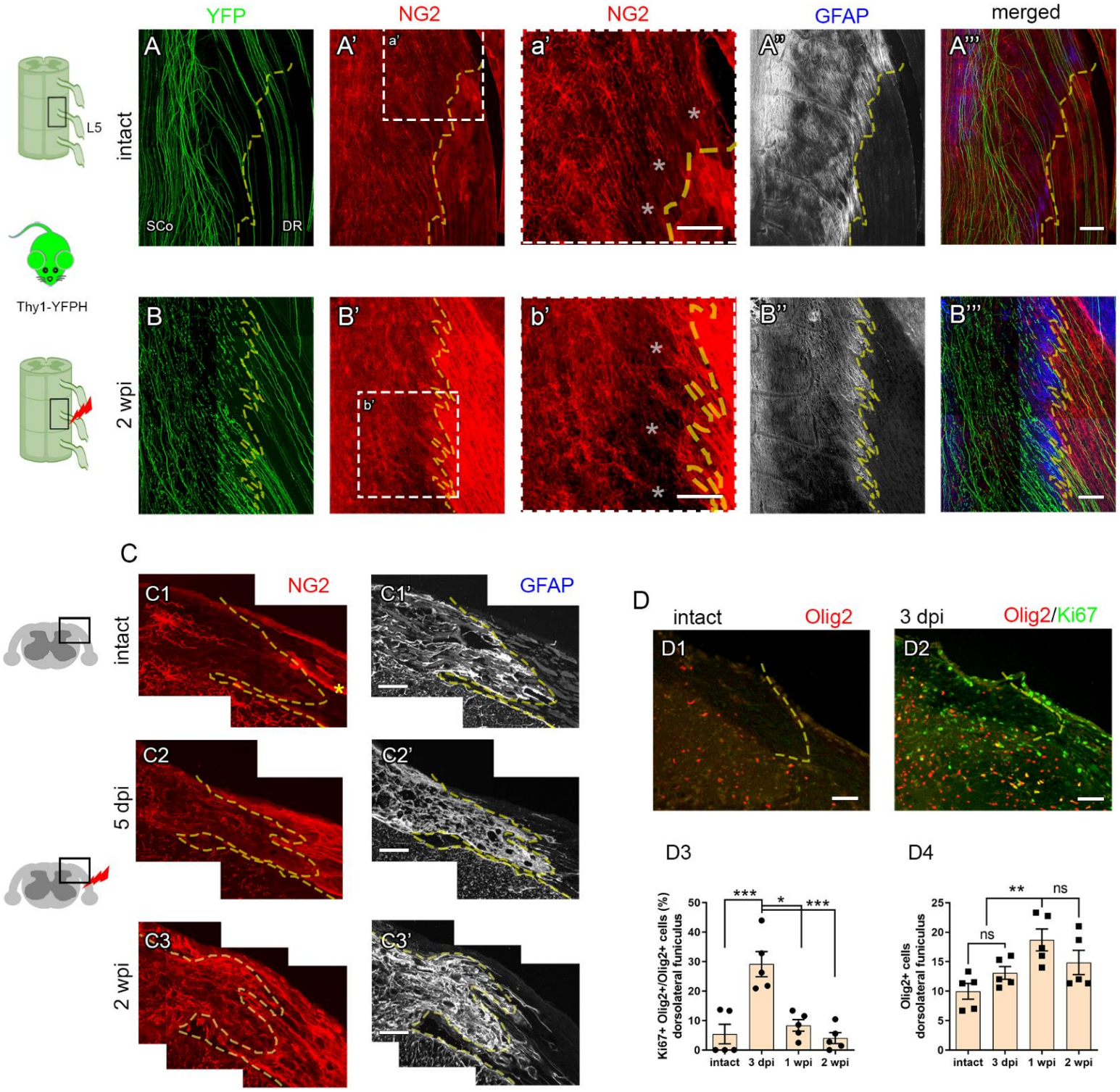

Figure S2. OPCs proliferate, migrate, and form a dense meshwork of processes after DR injury

(A, B) Wholemount views of intact (A) and axotomized (B) DREZ area showing subsets of YFP+ axons (A, B) and the distribution of NG2-labeled OPCs and their processes (A', B'). Dotted line approximates the borderline (dotted line) denoted by GFAP-labeled astrocytes (A", B"). Enlarged images (a', b') show area near the borderline (asterisks) and deeper in CNS territory. Scale bar: 100µm

(C) Transverse sections of intact (C1, C1') or axotomized DREZ at 5 dpi (C2, C2') and 2 wpi (C3, C3'), co-labeled for NG2 (C1-C3) and GFAP (C1'-C3'), illustrating temporal development of a dense meshwork of OPC processes populating the DREZ after DR injury. Scale bar: 50µm

(D) Quantification of OPC proliferation by counting nuclei colabeled by Olig2, a marker of OPCs and oligodendrocytes (D1), and Ki67, a marker of cell proliferation (D2), illustrating rapid proliferation of OPCs after DR injury that peaks at 3 dpi (D3) and doubles the number of Olig2+ cells by 1 wpi (D4). N= >3 sections/each mouse, 5 mice/each time point. Error bars represent SEM. p values are calculated by one-way repeated measures ANOVA with Tukey's post hoc test. ns, $p > 0.05$; *$p \leq 0.01$, **$p \leq 0.001$, ***$p \leq 0.0001$.

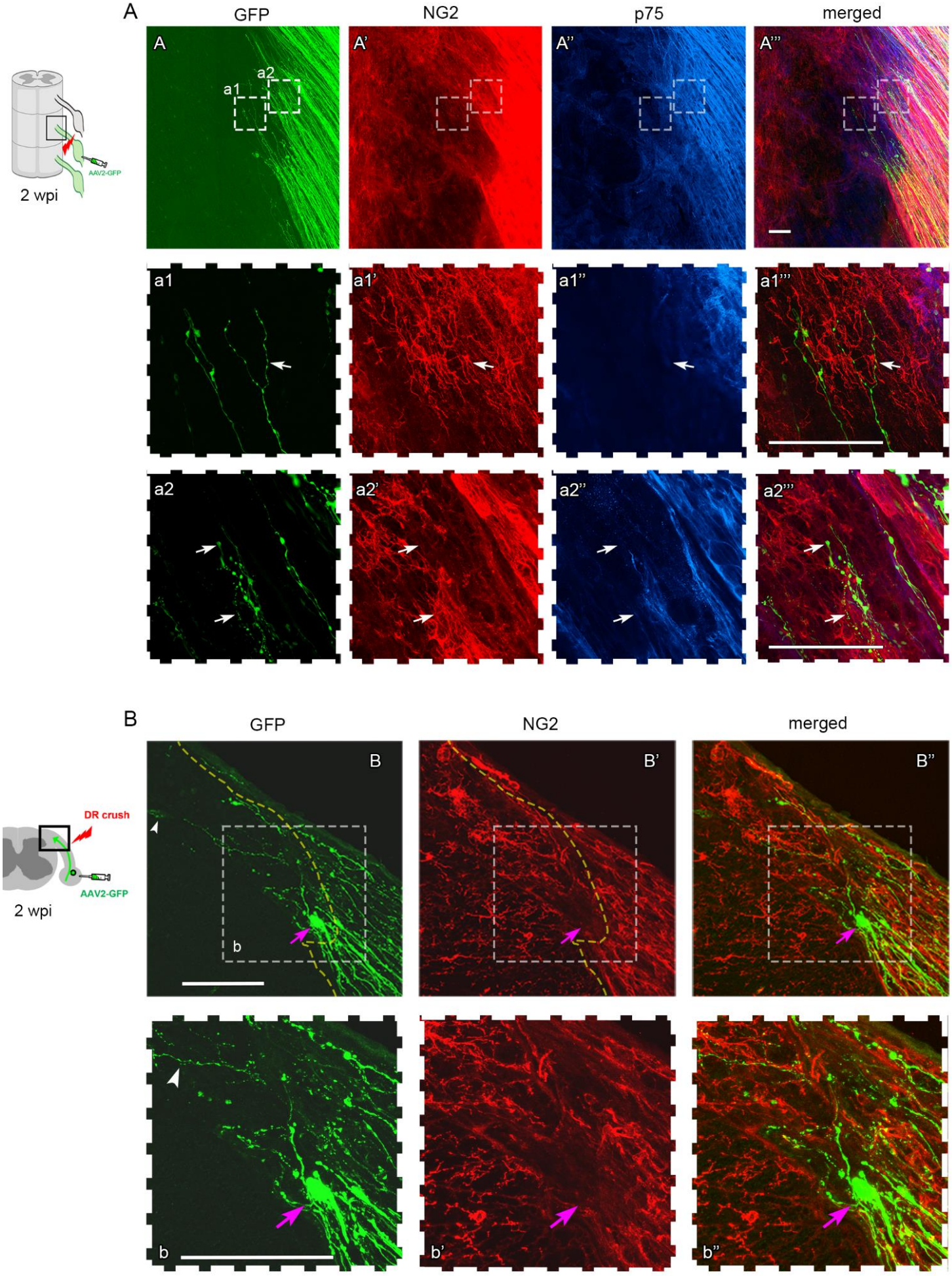
A
GFP
NG2
p75
merged
A
A'
A''
A'''
a1
a2
AAV2-GFP
2 wpi
a1
a1'
a1''
a1'''
a2
a2'
a2''
a2'''
B
GFP
NG2
merged
DR crush
AAV2-GFP
2 wpi
B
B'
B''
b
b
b'
b''

Figure 4. Stopped axons without dystrophic endings display extensive contacts with OPC processes

(A) Wholemount views of the DREZ area in low (A-A''') and high (a1-a2''') magnifications at 2 wpi, showing GFP+ axons (A, a1, a2), NG2-labeled OPCs (A', a1', a2'), and p75-labeled Schwann cells (A'', a1'', a2''). Arrows in enlarged views (a1-a2''') indicate examples of direct contact points between OPC processes and arrested axons. NG2 staining in the PNS is intense after DR injury but does not preclude identification of OPC processes. Scale bar: 100μm

(B) Transverse sections in low (B-B'') and high (b-b'') magnifications showing GFP+ axons (B, b) and NG2-labeled OPCs (B, b) at 2 wpi. Arrowheads indicate an example of many axons that stopped past the borderline (dotted line) in association with OPC processes. Arrows indicate a dystrophic ending formed at the borderline that, in contrast, lacks contacts with OPC processes. Scale bar: 50μm

Related data are available in **Figure S3**.

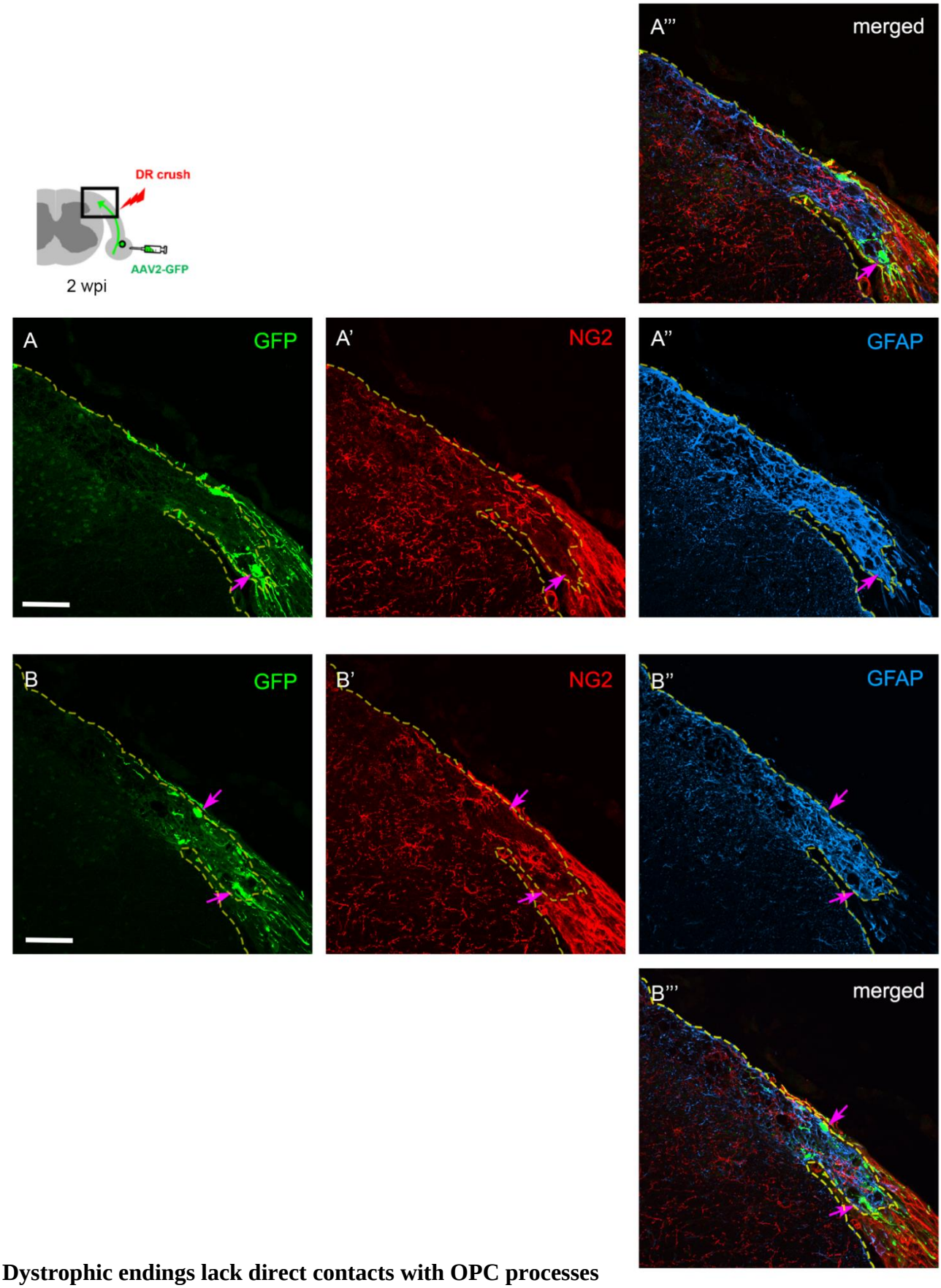

Figure S3. Dystrophic endings lack direct contacts with OPC processes
(A, B) Two transverse sections at 2 wpi, showing large bulbous endings (arrows) formed by some GFP+ axons (A, B) at the borderline (dotted line), NG2-labeled OPCs (A', B'), and GFAP-labeled astrocytes (A", B"). These putative dystrophic endings form where OPC processes are rare. Scale bar: 50μm.

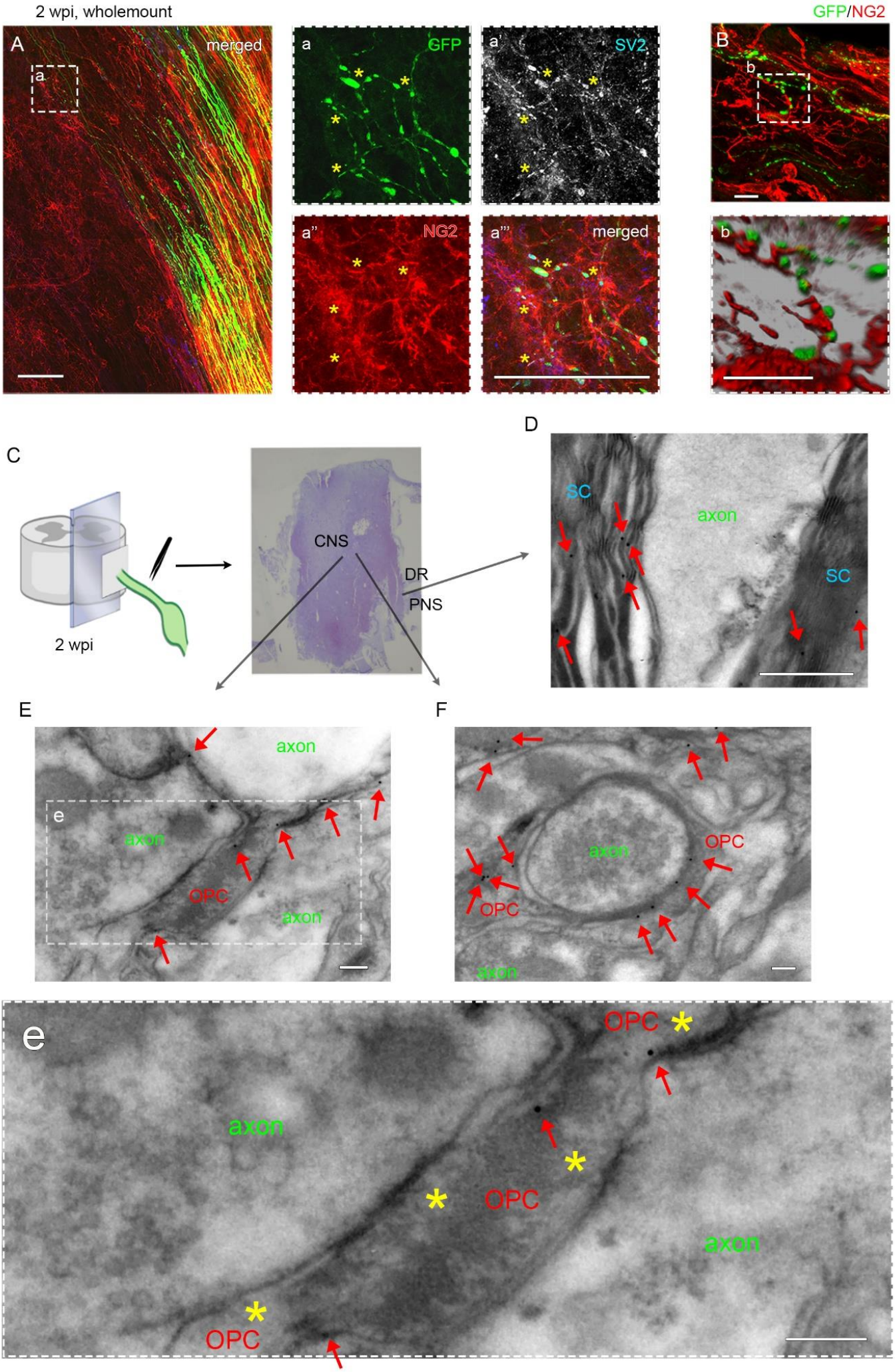
2 wpi, wholemount
A
merged
a
a
GFP
a'
SV2
GFP/NG2
B
b
a''
NG2
a'''
merged
b
C
2 wpi
CNS
DR
PNS
D
SC
axon
SC
E
axon
e
axon
OPC
axon
F
axon
OPC
OPC
axon
e
OPC
axon
OPC
axon
OPC

Figure 5. DR axons form synaptic endings on OPC processes

(A) Wholemount views of the DREZ area at 2 wpi in low (A) and high magnifications (a-a'''), showing GFP-labeled axons (a), SV2-labeled synaptic vesicles (a'), and NG2-labeled OPCs (a''). Boxed area in A shows several axons with small swellings on axon tips and shafts (a) intensely labeled for SV2 (a') and tightly associated with OPC processes (a''). Asterisks indicate same positions in a-a'''. Scale bar: 100μm (A), 50μm (a-a''')

(B) Volume rendered image (b) of a boxed area in B, illustrating direct contacts of axon swellings (Green) with OPC processes (Red). Scale bar: 5μm

(C) Diagram showing procedures to prepare a longitudinal vibratome slice of dorsal spinal cord with attached DR at 2 wpi.

(D) An electron micrograph of the PNS area showing gold particles (arrows) targeted to NG2 selectively labeling Schwann cells (SC). Scale bar: 500 nm

(E) An area of the DREZ showing that OPC processes denoted by gold particles (arrows) form synaptic contacts with axons. Magnified view of boxed area (e) illustrates synaptic contacts (asterisks) with presynaptic clustering of synaptic vesicles and thin postsynaptic density. Scale bar: 100 nm (E, e)

(F) An electron micrograph illustrating varicosity-like synaptic profile formed by DR axon encircled by OPC processes identified by gold particles (arrows). Scale bar: 100 nm

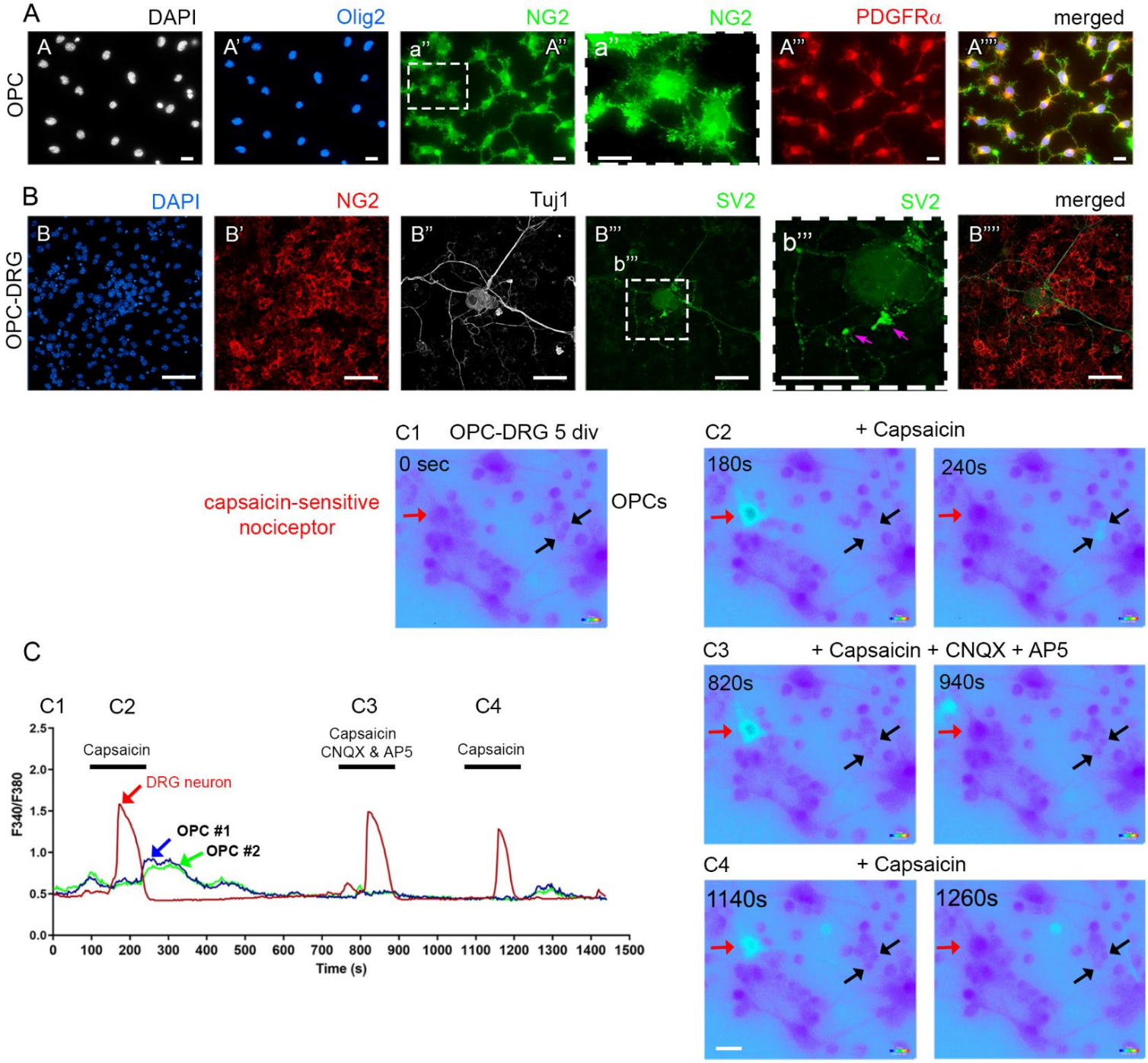

Figure 6. OPCs form functional synapses with co-cultured DRG neurons

(A) >95% pure OPCs, cultured from spinal cords of p16-18 mice, immunolabeled at 3 div for DAPI (A), Olig2 (A') and NG2 (A"), and PDGFRα (A'''). Enlarged view (a") of boxed area in A" illustrates OPCs with bushy processes resembling OPCs *in vivo*. Scale bar: 20µm

(B) Purified OPCs and DRG neurons co-cultured for 5 days, showing DAPI (B), NG2-labeled OPCs (B'), Tuj1-labeled axons (B"), and SV2-labeled synaptic vesicles (B'''). Magnified view (b''') of boxed area in B''' illustrates microtubule-deficient but SV2-enriched axonal swellings (arrows) formed on OPCs. Scale bar: 50µm

(C) Representative calcium imaging recordings of OPC-DRG neurons co-cultured for 5 days, illustrating temporal calcium responses of a neuron (red arrows) and two adjacent OPCs (black arrows), before (C1) and following capsaicin stimulation of neurons without (C2) or with antagonists of AMPA/kainate and NMDA receptors (C3), CNQX and AP5. Following washout of antagonists (C4), capsaicin stimulation of the same neuron again elicits calcium responses in the same OPCs. Scale bar: 30µm

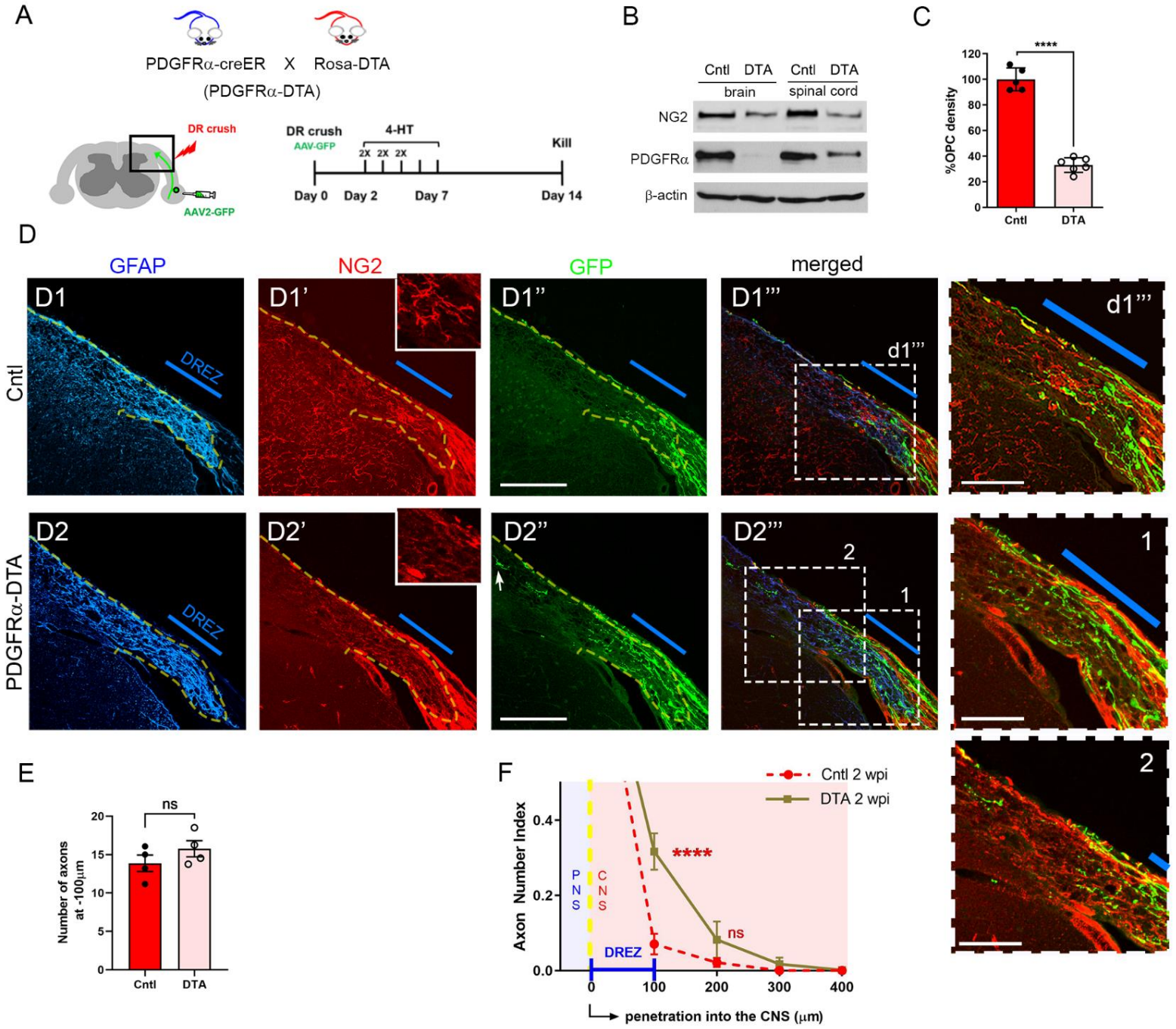

Figure 7. Genetic OPC ablation, although incomplete, markedly enhances axon regeneration

(A) Diagram illustrating experimental procedures to evaluate the effects of genetic OPC ablation at 2 weeks after C5-C8 root crush followed by AAV2-GFP injections to C5 and C7 DRGs.

(B) Western blotting showing markedly reduced markers of OPCs, NG2, and PDGFRα, in PDGFRα-DTA mice.

(C) Quantitative comparisons of OPC density measured by mean fluorescence intensity of NG2 staining in the spinal cord, illustrating ~70% ablation of OPCs in PDGFRα-DTA mice used for the analysis. Error bars represent SD. Unpaired t test (n=5 control, 6 DTA mice). ****$p \leq 0.00001$

(D) Transverse sections of a control (D1-D1''') and a PDGFRα-DTA mouse with ~80% OPC ablation (D2-D2''') at 2 wpi showing GFAP-labeled astrocytes (D1, D2), NG2-labeled OPCs (D1', D2'), and GFP+ axons (D1''', D2'''). Enlarged views of boxed area (d1''', 1, 2) illustrate that more axons cross the border and DREZ in the PDGFRα-DTA mouse. Blue lines approximate ~100μm wide region of the DREZ. Dotted lines denote borderline identified by GFAP staining. Insets in D1' and D2' are magnified views of the DREZ, illustrating residual and/or repopulating OPCs in PDGFRα-DTA mice. An

arrow in D2" denotes axons extending unusually deeply into the dorsal funiculus. Scale bar: 100μm (D1-D2'''), 50μm (d1''', 1, 2)

(E) Quantification of GFP+ axons at ~100μm proximal to the borderline in the PNS, illustrating insignificant difference between control and PDGFRα-DTA mice. Error bars represent SEM (n = 4 mice/group). Unpaired Student's t-test. ns, $p > 0.05$

(F) Quantitative comparisons of control and PDGFRα-DTA mice illustrating that OPC ablation, although incomplete, triples the number of axons extending past the DREZ. Error bars represent SEM (n=4 mice/group). Two-way repeated-measures ANOVA with Tukey's multiple comparisons test. 100μm, ****$p \leq 0.00001$; 200μm, ns, $p > 0.05$; 300μm

Related data are available in **Figure S4-S7**.

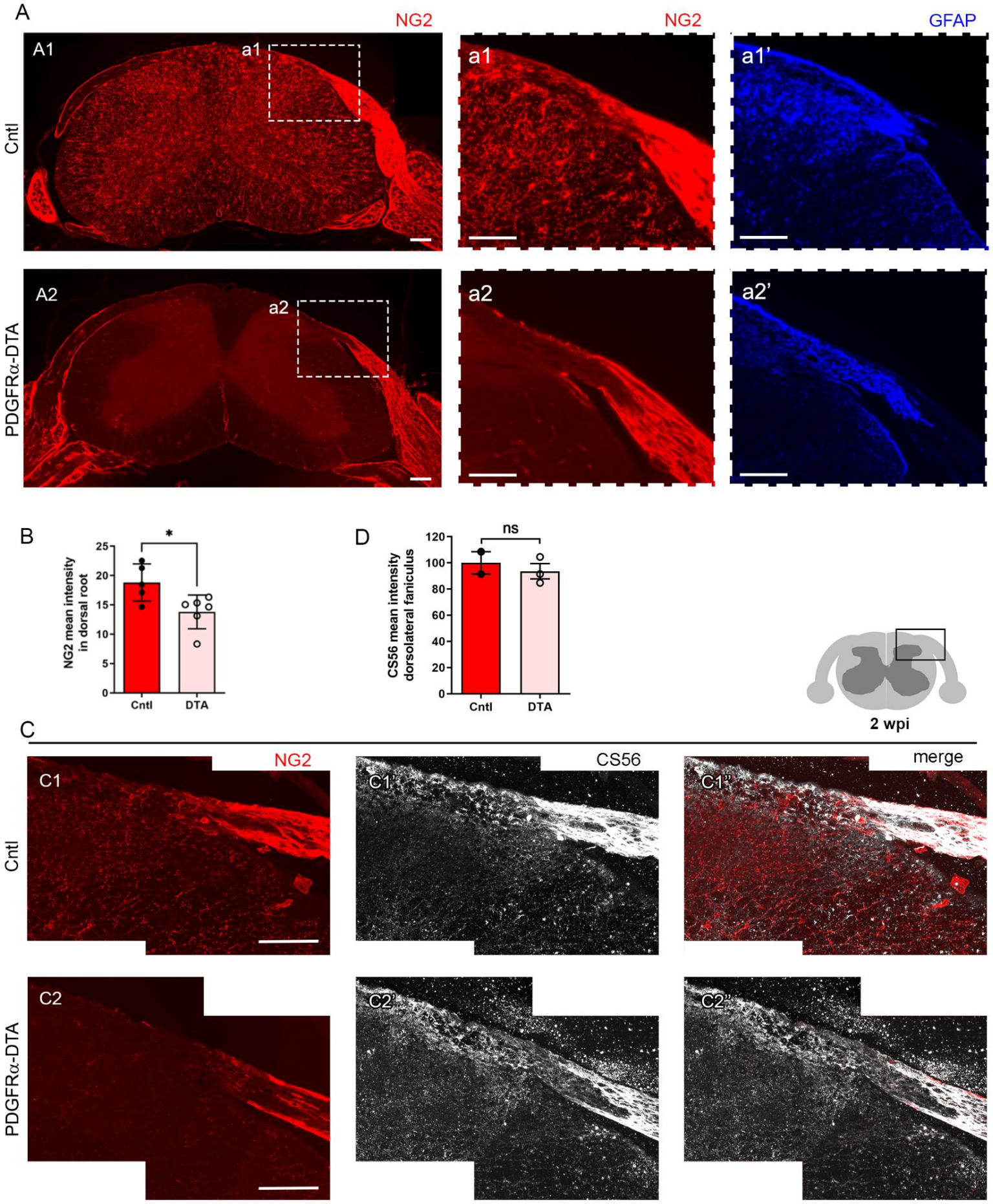
A
NG2
NG2
GFAP
A1
a1
a1
a1'
Cntl
A2
a2
a2
a2'
PDGFRα-DTA
B
*
NG2 mean intensity in dorsal root
25
20
15
10
5
0
Cntl
DTA
D
ns
CS56 mean intensity dorsolateral faniculus
120
100
80
60
40
20
0
Cntl
DTA
2 wpi
C
NG2
CS56
merge
C1
C1'
C1''
Cntl
C2
C2'
C2''
PDGFRα-DTA

Figure S4. Comparison of NG2/CSPG4 and CSPGs expression in control and PDGFRα-DTA mice

(A) Transverse sections of a control (A1) and a PDGFRα-DTA mouse with ~80% OPCs ablated at 2 wpi (A2), co-labeled for NG2 (a1, a2) and GFAP (a1', a2'), illustrating a marked reduction in OPCs and their processes in the spinal cord of the PDGFRα-DTA mouse. Enlarged views of the boxed area in A1 and A2 show slightly reduced NG2 immunostaining peripherally along the DR of the PDGFRα-DTA mouse (a2), as compared to control mouse (a1). Scale bar: 100μm

(B) Quantitative comparisons of control and PDGFRα-DTA mice, illustrating a slight reduction of NG2 immunoreactivity in dorsal roots of DTA mice. Unpaired Student's-t test (n=5 control, 6 DTA mice). Error bars represent SEM. *$p \leq 0.01$

(C) Transverse sections of a control (C1-C1") and a PDGFRα-DTA mouse (C2-C2"), co-labeled for NG2 (C1, C2) and for CS56 (C1', C2') at 2 wpi, showing reduced NG2 but abundant CSPGs associated with the DREZ area of DTA mice. Scale bar: 100μm

(D) Quantitative comparisons of control and PDGFRα-DTA mice, illustrating insignificant difference in CS56 immunoreactivity measured in the dorsolateral funiculus including the DREZ. Unpaired Student's t-test (n=2 control, 3 DTA mice). Error bars represent SEM. ns, $p > 0.05$

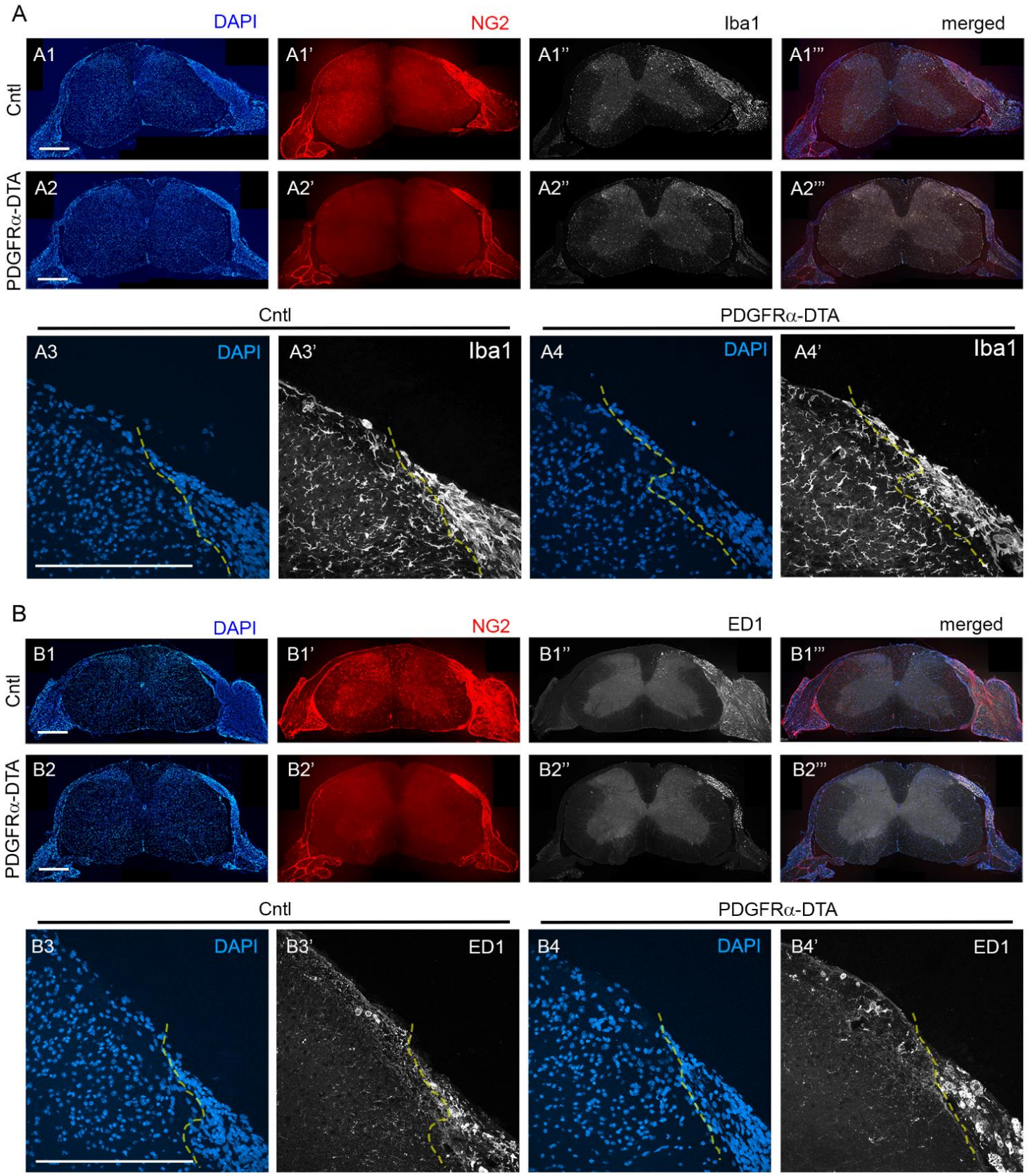
A
DAPI
NG2
Iba1
merged
Cntl
PDGFRα-DTA
A1
A1'
A1''
A1'''
A2
A2'
A2''
A2'''
Cntl
PDGFRα-DTA
A3
DAPI
A3'
Iba1
A4
DAPI
A4'
Iba1
B
DAPI
NG2
ED1
merged
B1
B1'
B1''
B1'''
B2
B2'
B2''
B2'''
Cntl
PDGFRα-DTA
B3
DAPI
B3'
ED1
B4
DAPI
B4'
ED1

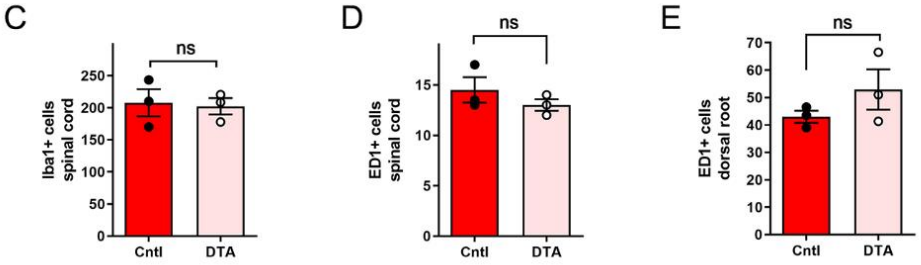
C
ns
Iba1+ cells spinal cord
250
200
150
100
50
0
Cntl
DTA
D
ns
ED1+ cells spinal cord
15
10
5
0
Cntl
DTA
E
ns
ED1+ cells dorsal root
70
60
50
40
30
20
10
0
Cntl
DTA

Figure S5. Comparison of microglia and macrophages in control and PDGFRα-DTA mice

(A) Transverse sections of a control (A1-A1''', A3 and A3') and a PDGFRα-DTA (A2-A2''', A4 and A4') mouse at 2 wpi, showing DAPI, NG2-labeled OPCs, and Iba1-labeled microglia, and illustrating no noticeable differences in morphology or density of microglia in the spinal cord, DREZ, or DR of control and DTA mice. Scale bar: 500μm

(B) Transverse sections from a control (B1-B1''', B3 and B3') and PDGFRα-DTA (B2-B2''', B4 and B4') mouse at 2 wpi, showing DAPI, NG2-labeled OPCs, and ED1-labeled macrophages, and illustrating no noticeable differences in the distribution or density of macrophages in the spinal cord, DREZ, or DR of control and DTA mice. Scale bar: 500μm

(C) Quantitative comparisons of control and PDGFRα-DTA mice illustrating insignificant difference in the number of Iba1+ microglia in the spinal cord. Unpaired Student's t-test (n=3 mice/group). Error bars represent SEM. ns, $p > 0.05$

(D, E) Quantitative comparisons of control and PDGFRα-DTA mice, illustrating insignificant difference in the number of ED1+ macrophages in the spinal cord (D) or dorsal root (E). Unpaired Student's t-test (n=3 mice/group). Error bars represent SEM. ns, $p > 0.05$

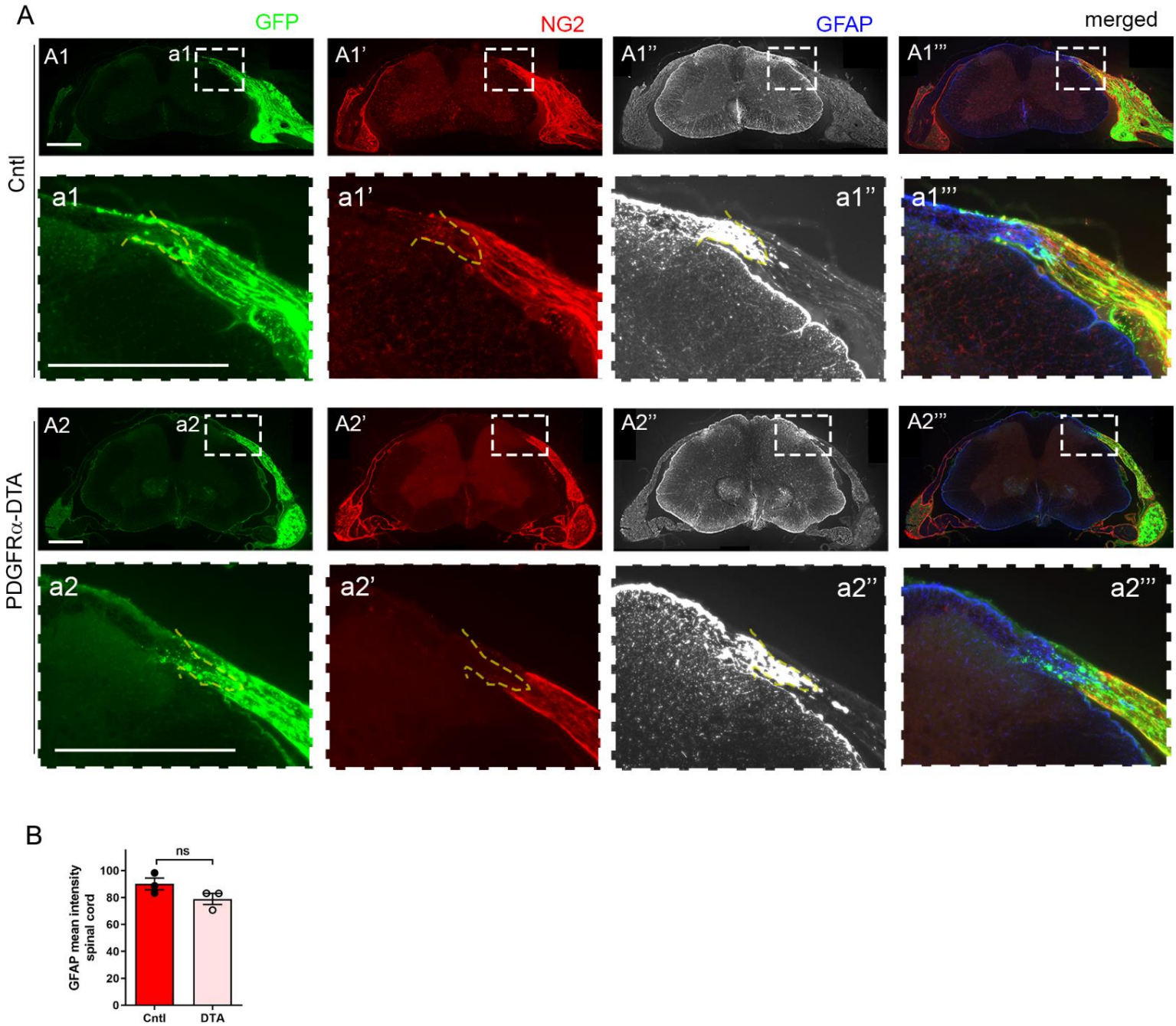

Figure S6. Comparison of astrocytes in control and PDGFRα-DTA mice

(A) Transverse sections of control (A1-a1''') and PDGFRα-DTA (A2-a2''') mice at 2 wpi, co-labeled for NG2 and GFAP, illustrating no noticeable differences in the density or distribution of astrocytes at the DREZ or within the spinal cord between control and DTA mice. Scale bar: 500μm

(B) Quantitative comparisons of control and PDGFRα-DTA mice, illustrating insignificant difference in the number of ED1+ macrophages in the spinal cord. Unpaired Student's t-test (n=3 mice/group). Error bars represent SEM. ns, $p > 0.05$

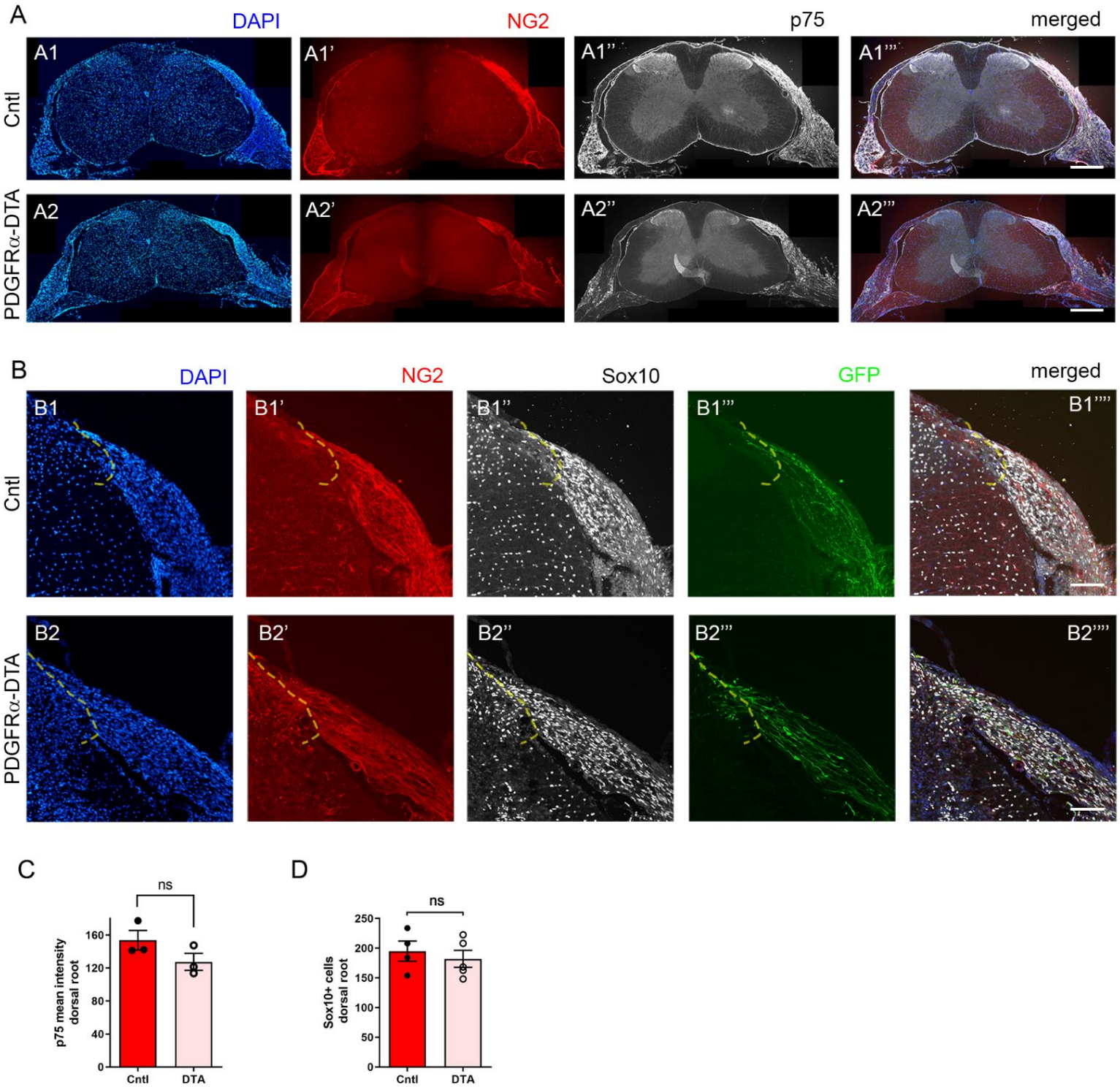

Figure S7. Comparison of Schwann cells in control and PDGFRα-DTA mice

(A) Transverse sections of control (A1-A1'''') and PDGFRα-DTA (A2-A2'''') mice at 2 wpi, illustrating that p75 immunoreactivity in dorsal root of DTA mouse is comparable to that of control mouse. Scale bar: 500µm

(B) Transverse sections of control (B1-B1'''') and PDGFRα-DTA (B2-B2'''') mice at 2 wpi, illustrating no noticeable difference in the number of Sox10-labeled Schwann cells present in the dorsal root. Scale bar: 100µm

(C) Quantitative comparison of control and PDGFRα-DTA mice, illustrating insignificant difference in p75 immunoreactivity in the dorsal root. Unpaired Student's t-test (n=3 mice/group). Error bars represent SEM. ns, $p > 0.05$

(D) Quantitative comparison of control and PDGFRα-DTA mice, illustrating insignificant difference in the number of Schwann cells in the dorsal root. Unpaired Student's t-test (n= 4 control, 5 DTA mice). Error bars represent SEM. ns, $p > 0.05$

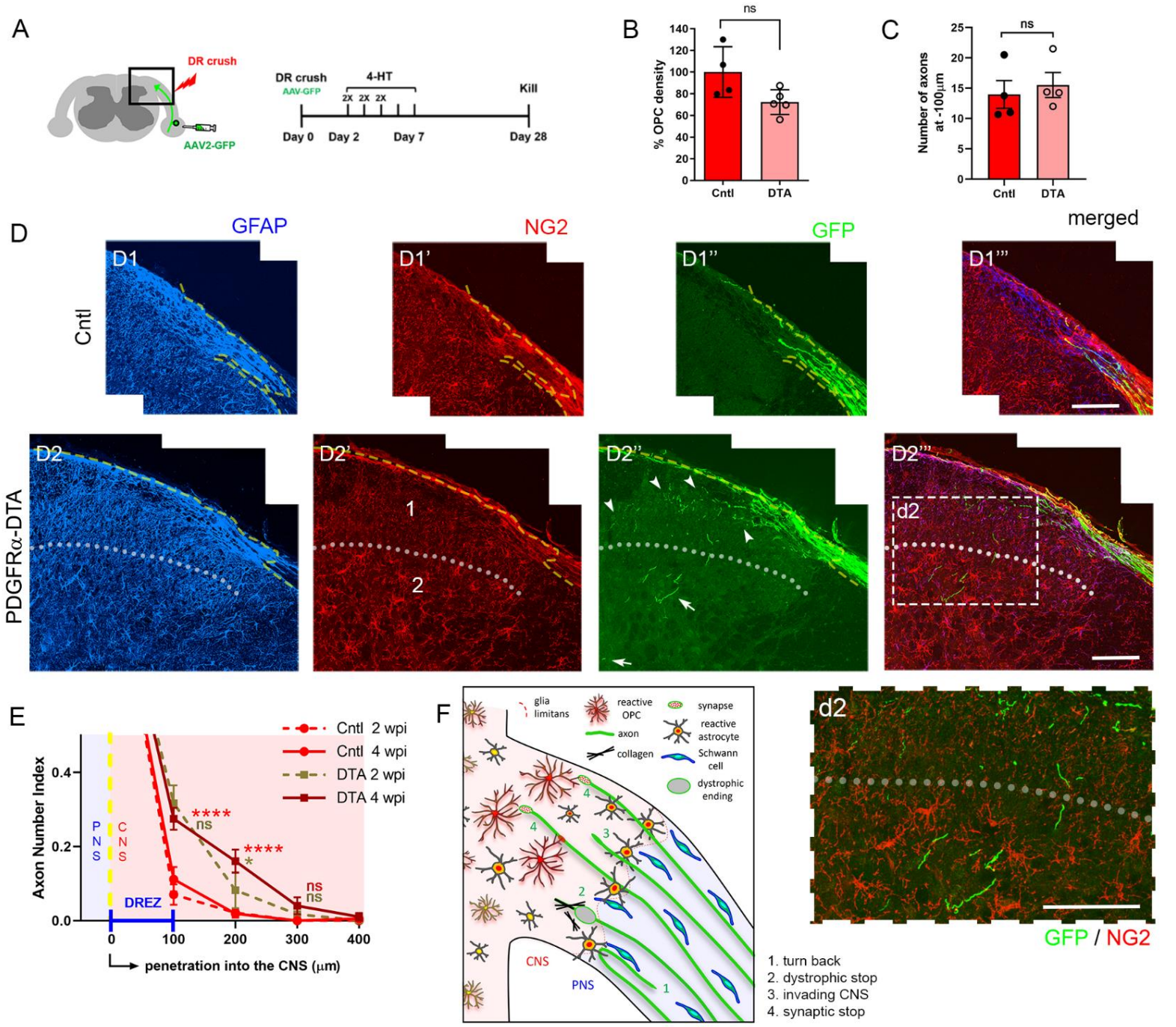

Figure 8. Axons continue regenerating intraspinally through areas lacking OPCs

(A) Diagram illustrating experimental procedures to evaluate the effects of genetic OPC ablation at 4 weeks after C5-C8 root crush followed by AAV2-GFP injections into C5 and C7 DRGs.

(B) Quantitative comparison of OPC density, measured by mean fluorescence intensity of NG2 staining in the spinal cord, illustrating ~30% ablation of OPCs in PDGFRα-DTA mice used for the analysis. Error bars represent SD. Unpaired t test (n=4 control, 5 DTA mice). ns, $p > 0.05$

(C) Quantification of GFP+ axons at ~100µm proximal to the borderline, illustrating insignificant difference between control and PDGFRα-DTA mice. Error bars represent SEM (n = 4 mice/group). Unpaired Student's t-test. ns, $p > 0.05$

(D) Transverse sections from a control (D1-D1''') and a PDGFRα-DTA mouse (D2-D2'''), illustrating massive repopulation of OPCs (D2') and GFP+ axons that regenerate remarkably deeply into the dorsal horn (D2''; arrows). There are noticeably fewer OPC processes where more axons (arrowheads) regrow within the spinal cord (area 1 in D2') than where fewer axons (arrows) regenerate (area 2 in D2''). Enlarged view of boxed area in D2'' illustrates regenerated GFP+ axons in association with repopulated OPC meshwork (d2). Scale bar: 100µm

(E) Quantitative comparison of control and PDGFRα-DTA mice illustrating that ~20% axons continue to regenerate past the DREZ in DTA mice during the additional two weeks. The number of axons counted at 100μm past the borderline remains unchanged at 4 wpi in DTA mice. Error bars represent SEM (n=4 mice/group). Two-way ANOVA with Sidak's multiple comparisons test. 100μm; ns, $p > 0.05$ (DTA 4 wpi vs. DTA 2 wpi); ****$p \leq 0.00001$ (DTA 4 wpi vs. control 4 wpi), 200μm; ****$p \leq 0.00001$ (DTA 4 wpi vs. control 4 wpi), *$p \leq 0.01$ (DTA 4 wpi vs. DTA 2 wpi), 300μm; ns, $p > 0.05$ (DTA 4 wpi vs. control 4 wpi, DTA 2 wpi).
(F) Schematic illustration of the proposed model of how DR axons terminate regenerating at the DREZ, highlighting OPCs as a major regenerative barrier.
Related data are available in **Figure S8**.

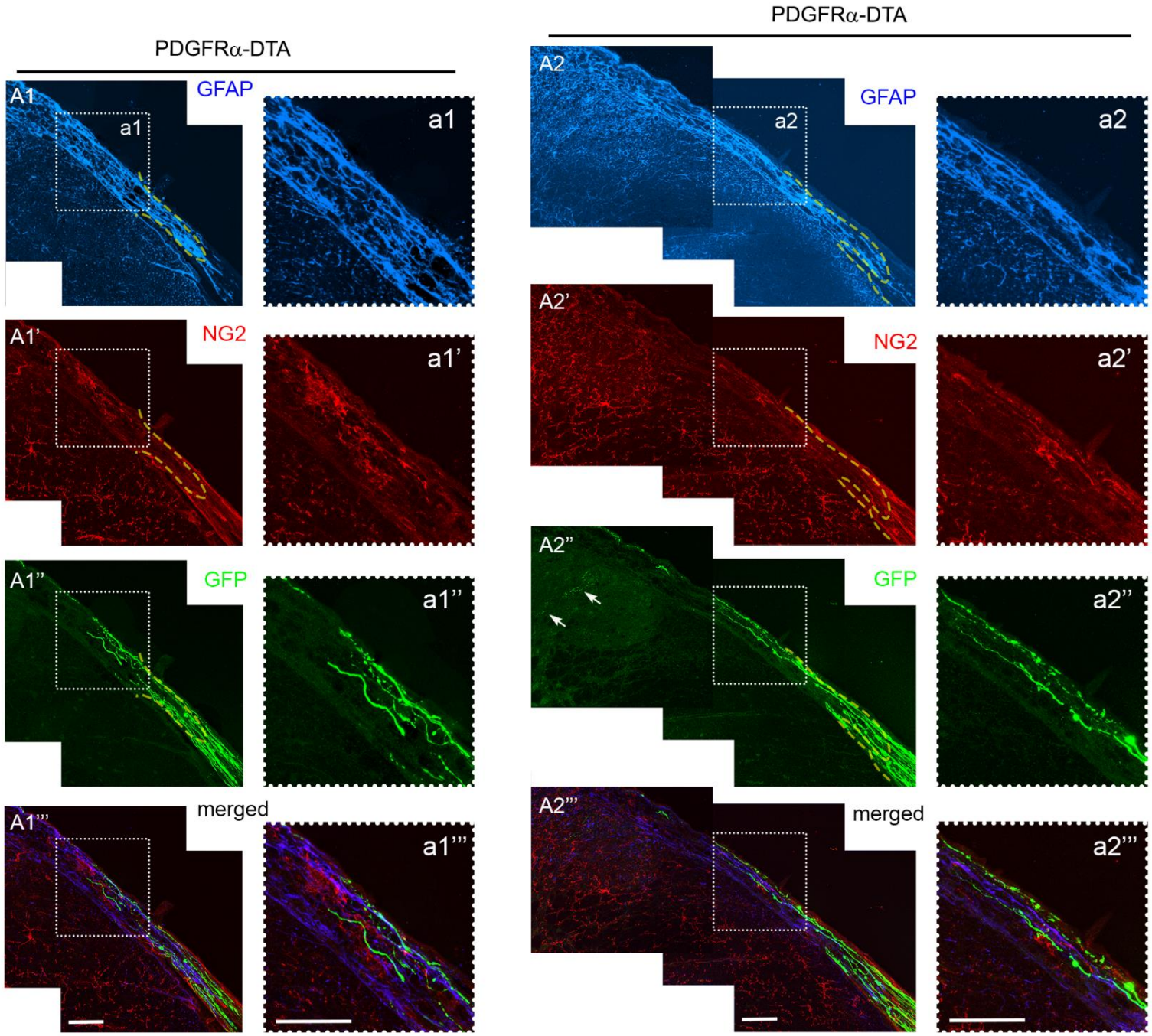

Figure S8. **Axons regenerate deeper into the dorsal funiculus in PDGFRα-DTA mice at 4 wpi (A1-A1''', A2-A2''')** Two sets of transverse sections of PDGFRα-DTA mice at 4 wpi, co-labeled for GFAP and NG2, illustrating more numerous GFP+ axons (A1", A2") that regenerated deeper into the dorsal funiculus than at 2 wpi (refer to Figure 7D2"). These axons terminate where OPCs are locally repopulated, in association with OPC processes (A1', A2'). Enlarged views of boxed area (a1-a2"') also indicate sparse distribution of OPCs where these axons regenerate. Arrows in A2" show axons reaching more deeply into the dorsal horn. Scale bar: 50μm